Does Scatter Matter? Improved Understanding of UH-60A Wind Tunnel Rotor Measurements Using Data-Driven Clustering and CREATE^{TM}-AV Helios

Manikandan Ramasamy **Rohit Jain**
Aerospace Engineers
U.S. Army Combat Capability Development Command
Aviation & Missile Center, Moffett Field, CA

Thomas R. Norman
Aerospace Engineer
NASA Ames Research Center
Moffett Field, CA

ABSTRACT

A data-driven clustering algorithm based on proper orthogonal decomposition was applied to assess the scatter found in the UH-60A wind tunnel airloads measurements. Upon verifying the capability of the algorithm, pushrod loads, blade surface pressure, sectional loads, and torsional moments were analyzed. Spatial eigenmodes resulting from the decomposition provided the optimal basis; projection of the individual cycles on to the high singular value modes allowed visualizing the statistical distribution of data over the entire azimuth. While not all cases showed furcation in the data, bimodal distribution was found in the high thrust cases, where statistically normal distribution is generally assumed. Consequent clustering of the measured cycles produced excellent correlation among clusters found in the pushrod loads, blade surface pressure, and torsional moment that suggest a common source for furcation in the data. The cycles assigned to one group repeatedly showed distinguishable variations from the other group in terms of the presence/absence of a dynamic stall vortex, azimuthal occurrence of stall, chordwise location of separation and reattachment etc. When one of the cluster is smaller in size compared to the other, the conventional phase-average obscured all the intricate features even when the loads are substantially higher than the larger cluster. In general, clustering the data set when warranted showed not only higher peak loads but also lower variance for both the clusters across the entire azimuth compared to the conventional simple phase-average results. Computational simulations were conducted using CREATE^{TM}-AV Helios towards understanding the underlying flow field. Misjudged earlier as under/over-predictive when compared with the simple phase-average data, Helios results consistently showed significantly improved correlation with the smaller of the two clusters. Combining the clustered results and the flow visualization provided by Helios, aperiodicity in the spatial location and the strength of both the trim tab vortices and tip vortices have also been hypothesized as potential sources of furcation.

NOTATION

α	angle of attack, deg
α_{max}	maximum angle of attack, deg
μ	advance ratio
θ_0	collective pitch, deg
$\theta_1 c$, $\theta_1 s$	collective pitch harmonics, deg
ψ	azimuth angle, deg
ψ_p	peak load azimuth, deg
σ	standard deviation
c_l	lift coefficient
c_m	moment coefficient
c_p	surface pressure coefficient
C_T	coefficient of thrust
r	radial station
R	Radius of the rotor blade
s	solidity
S	singular values
U	spatial eigenmode
V	time coefficients

Acronyms:

2D, 3D	two- and three-dimensional
APR	all pushrods
ASAS	all sensors - all stations
AS1S	all sensors - 1 station
B1, B2, B3, B4	blades 1, 2, 3, and 4, respectively
CA1	cluster averages of group 1 cycles
CA2	cluster averages of group 2 cycles
JPDF	joint probability density function
NDC	n-Dimensional clustering
POD	proper orthogonal decomposition
PR1, PR2, PR3, PR4	pushrod 1, 2, 3, and 4, respectively
SPA	simple phase-average

Presented at the Vertical Flight Society's 77th Annual Forum & Technology Display, Virtual, May 10–14, 2021.

INTRODUCTION

Conducting a full-scale rotor test or flight test is both challenging and cost expensive. When combined with the signifi-

cance of such measurements in terms of data usage for design and validation, reducing uncertainties in the measurements becomes imperative. Generally, experimental measurement of any phenomena exhibit scatter. In the case of rotor measurements, scatter appears in the form of cycle-to-cycle variations in the measured loads. Reducing uncertainty through accurate representation of scatter is, therefore, essential for confident application in rotor design as well as to validate the predictive accuracy of computational simulations.

Historically, assuming a statistically normal distribution in the scatter, mean and variance are used to represent the data. For example, pitching airfoil studies aimed at understanding rotor dynamic stall were represented using simple phase-averages (SPA) and standard deviation (Ref. 1–3). Variations in the measurements caused by flow field turbulence, which is inherently random, justifies applying SPA. However, recent pitching airfoil experiments showed that the data scatter is not completely random (Ref. 4). The cycle-to-cycle variations of surface pressure, lift, moment, and drag coefficients measured over the entire oscillation cycle fell under two or three groups, suggesting a bi- or tri-furcated data.

Furcation refers to the measured parameters such as lift or moment occurring in clusters instead of exhibiting a statistically normal distribution. For reference, general characteristics of clusters are that the clusters (1) are discernible, (2) exhibit statistically significant differences in the measured loads among them, and (3) are caused by different flow conditions (or from the aeroelastic response of the blade). While the difference between the clusters should be significant, the cycles within each cluster must be similar. One such example is when the flow shows the presence of a dynamic stall vortex in some cycles that are absent in others for the same applied forcing function (Ref. 5). The former set of cycles produce significantly higher loads through lift augmentation compared to the latter set; thereby forming two distinct clusters in the measured loads (Ref. 4). Historical application of SPA and variances are appropriate when the data distribution is statistically normal. However, the consequences of ignoring the presence of clusters on a bimodal data were found to be high; SPA obscured majority of the important flow phenomena at best, and produced severe under-determination of airloads that are critical to designing helicopter components such as pushrods (Refs. 4).

Evidences for a furcated data exist in experiments that were conducted at different research facilities using different airfoils (or wings) at different Mach numbers and, in general, different operating conditions (Refs. 4, 6–8). Ramasamy et al. (Ref. 4) showed several factors contributing to the data furcation in pitching airfoil experiments using VR7 and modified VR12 airfoils. The factors include variations in the: (1) chordwise location of separation, (2) phase occurrence of dynamic stall, (3) strength of the dynamic stall vortex, (4) presence/absence of dynamic stall vortex, etc. It was recommended in Ref. 4 that cluster-averages (CA) and associated cluster-variances be determined to represent each cluster present in the data, as opposed to the conventional SPA. For reference, cluster-averages are phase-averages determined using all the cycles that belong to a cluster.

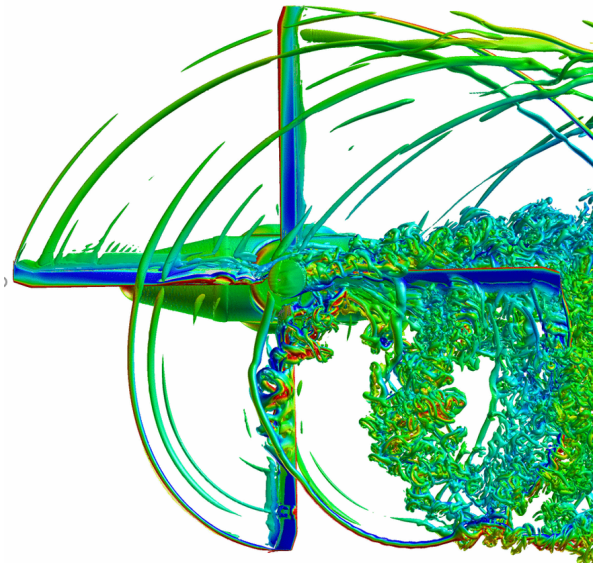

Figure 1. Complex flow field of UH-60A rotor simulated using Helios

A question that immediately followed the observed furcation in 2D airfoil and 3D finite-wing experiments, which formed the motivation for the present study, is the probable occurrence of furcation in rotor measurements. Rotors produce one of the most complex flow field. Figure 1 shows the flow field of a UH-60A simulation made using Helios corresponding to one of the test case analyzed in this study (R45P36). As the blade spins, it encounters tip vortices trailing from the preceding blade(s), vortex sheets, and root vortices, hub wake etc. Tip vortices are known to trigger stall and their proven aperiodicity (in terms of strength and the spatial location relative to the blade) can enable furcation in the data set. Such complex flow can produce more than two groups in the data, i.e., tri- or quad-furcation.

The primary objective of the present work is to analyze the scatter found in one of the most widely used full-scale rotor experiments, i.e., the UH-60A airloads test (Ref. 9), conducted at the National Full-Scale Aerodynamics Complex (NFAC). High-speed, high-thrust conditions are targeted for stall and separation related furcation. The presence of clusters in the data are assessed using an in-house developed, data-driven, optimal-basis clustering algorithm called n-Dimensional Clustering (NDC). In cases that warrant grouping, correlation studies are conducted among multiple measurement parameters (such as blade surface pressure, sectional loads, pushrod loads, and torsional moments) to ascertain the presence of clusters. Once confirmed, cluster-averages, variances, and probability of occurrence of each cluster are determined. The resulting cluster-averages are an improved representation of the measured airloads with reduced uncertainty than the conventional SPA results. Lastly, upon correlating Helios with the clustered results, simulated flow fields that showed good correlation are used to iden-

tify and understand various aerodynamic phenomena that may have contributed to the formation of clusters.

UH-60A DATA SET

A comprehensive test measuring both the airloads and the structural loads on a four-bladed, full-scale UH-60A rotor was conducted at the NFAC wind tunnel (Ref. 9). Airloads were measured on blade 1 (B1) using surface pressure sensors mounted at nine radial stations from as inboard as $r/R = 0.2$ to as outboard near the tip as $r/R = 0.99$, where R is the radius of the blade. Each station carried 18 to 25 sensors that are distributed along the chord. Figure 2 shows the location of surface pressure sensors as mounted on the UH-60A rotor blade. Sectional loads, such as c_l, c_m, and c_d were determined by integrating surface pressure at corresponding radial stations. Pushrod loads and sectional structural loads were measured using strain gauges. While all four pushrods were instrumented, structural loads were only measured using blade 3 (B3). Optical measurements were also employed to study rotor wake and blade deflection (Ref. 10, 11). Details of the experiment including the set up, instrumentation, and the acquired data are given in Ref. 9.

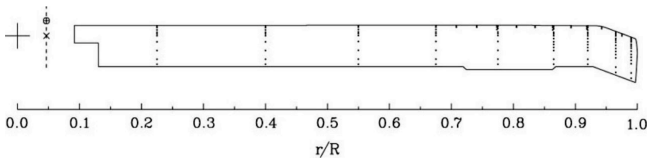

Figure 2. UH-60A blade surface pressure sensor locations

The present study uses three kinds of data, in general: (1) push rod loads, (2) surface pressure and other derived sectional loads measured on blade 1, and (3) torsional moment on blade 3. Among other structural measurements, torsional moment is of most interest as it allows correlation with pushrod loads. In all the cases, data was acquired for a total of 128 cycles. Both the pushrod loads and torsional moment were measured at 256/rev. Blade surface pressure data was acquired at a much higher frequency, i.e., 2048/rev. Four specific test points relating to a thrust-sweep run (listed in Table 1) are chosen for analysis. Considering all four cases produced high thrust, P35 and P36 are referred to as lower thrust cases, and P37 and P38 as higher thrust cases throughout the analysis. While points 37 and 38 have very similar blade loading (C_T/s), they differed in the collective and cyclic pitch settings needed to trim the rotor.

Table 1. Test cases and relevant operating conditions

Run	Pt.	Mach	μ	C_T/s	θ_0	θ_{1c}	θ_{1s}
45	35	0.3	0.125	0.1104	9.1	2.1	-6.90
45	36	0.3	0.125	0.1203	10.4	2.8	-8.40
45	37	0.3	0.125	0.1253	11.9	3.6	-10.2
45	38	0.3	0.125	0.1255	12.3	3.8	-10.6

Preliminary Assessment: All Pushrod Data

Preliminary analysis is conducted to identify data with known multi-modal characteristics. Such data set provides explicit and irrefutable information necessary to validate the applied clustering algorithm. To begin with, analysis is conducted on the highest thrust case (R45P38) that exhibited dynamic stall characteristics.

Raw data from all the four pushrods are shown in Figs. 3a and b; the latter is color coded to separate the data among pushrods. One of the biggest challenges in plotting all the data simultaneously (Fig. 3d) is that it obscures the data distribution. Visually, joint probability density function (JPDF) can provide a better assessment of the distribution. JPDF first bins both the azimuth (x-axis) and the load (y-axis), then counts the number of cycles contributing to each bin. A brighter bin refers to contribution from more cycles. JPDF results in Fig. 3c shows two distinct paths at the peak load azimuth (about 240°). Approximately equal brightness for both the paths suggest two equal-sized groups of loads being present in the data.

Simple phase-average (SPA) determined from all the 128 cycles for each pushrod is shown in Fig. 3d. Consistent with the JPDF, two groups are seen. PR1 and PR3 form the first group while PR2 and PR4 form the second group. The difference between the two groups is vivid on the retreating side, beginning with the waveform at around 180° azimuth. While the pushrods corresponding to the instrumented blades (PR1 and PR3) have a single peak (local peak), pushrods attached to the un-instrumented blades (PR2 and PR4) show a dual-peak. At the location of the overall peak load (about 240° azimuth), the data from instrumented blades show an average of about 3400 lbs while the average peak of the un-instrumented blades is around 2700 lbs.

Such groups among the pushrods is a result of the structural property differences (and the associated aeroelastic response) between the instrumented (B1 and B3) and the un-instrumented (B2 and B4) blade sets (Ref. 12). Nevertheless, it is these explicit differences in loads and wave forms that are needed to validate the applied clustering algorithm.

CLUSTERING ALGORITHM

In this section, a brief introduction to the in-house developed clustering algorithm and the associated steps are discussed. The algorithm begins with evaluating the nature of the data. Typically, assessments on normality can be conducted relatively easily using the Hartigans dip test (Refs. 13, 14). If the data exhibits statistically normal distribution, the process ends with determining SPA and variance. In the present study, challenge begins at the first step itself, where the data distribution must be studied over the entire azimuth simultaneously. As seen earlier, JPDF provides the density distribution at each azimuth. However the results can be contradicting when the results are assessed at different azimuths. For example, Fig. 3c showed bimodal distribution between 0° and 45°,

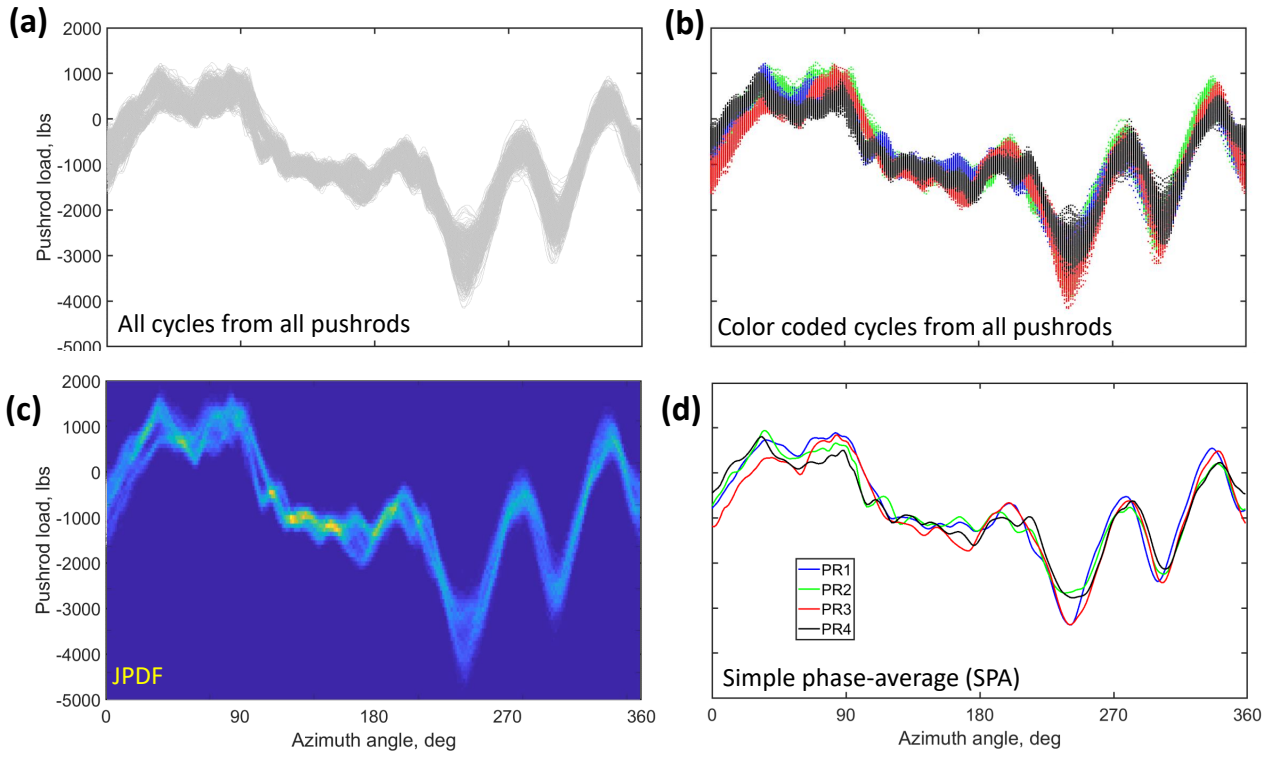

Figure 3. Data from all cycles for all pushrods

and at the peak load azimuth (240°). The same figure, however, showed normal distribution (one bright path) between 90° and 180°. Such contradicting information is not helpful in normality analysis. The ability to connect all azimuths, i.e., to treat the load variation over the entire azimuth for a given cycle as a single data point is necessary.

Proper orthogonal decomposition (POD) provides the solution via dimensionality reduction, and forms the core of the applied clustering methodology. The resulting spatial modes are the basis over which the analysis is conducted. Details of the clustering algorithm, referred to as n-Dimensional clustering (NDC) are explained in detail in Refs. 4, 15. NDC starts with the application of POD such that

$$[X] = U\ S\ V^T \tag{1}$$

where X can be any of the data matrix shown in Table 2. For example, pushrod 1 loads (first row in Table 2) will have a data matrix of 256 $\times$ 128. The 256 rows represent the azimuthal angles at which the data is taken and the 128 columns correspond to the number of acquired cycles. When all the four pushrods are used, the number of columns increase to 128 $\times$ 4. The decomposition of the mean centered data results in three vectors: U is the spatial mode, S is the singular value (significance of each mode in the data se), and V^T represent the time coefficient (or the projection of individual cycles onto the spatial modes).

The number of modes for clustering is selected based on the singular values. Using only the first mode (highest singular value) means only the differences at the highest level must be taken into account. Adding more modes begins including smaller differences among cycles to be accounted while determining the number of clusters in the data. Understandably, when all the modes are used, each individual cycle forms its own cluster. For the present study, by limiting the number of modes to one or two, high frequency variations are prevented in contributing to the determination of clusters.

Clustering analysis is conducted on the time coefficients of the selected modes, which quantify the magnitude of the spatial modes present in each of the individual cycles. Existing algorithms such as k-means (Ref. 16), hierarchical agglomerative clustering (Ref. 17), t-SNE (Ref. 18) etc. use Euclidean distance or Manhattan distances, which are prone to error from high frequency oscillations. Also, all the other methods require the user to determine the number of groups present in the data. NDC algorithm objectively determines the number of clusters by counting the number of peaks present in the n-Dimensional histogram of time coefficients, without subjective interpretation. The latter is very important because even a normally distributed data can be forced to produce clusters in other algorithms through incorrect user judgement of the number of groups. However, NDC algorithm inherently cannot cluster a data set that exhibits normal distribution.

Once the number of clusters are ascertained, individual cycles

Table 2. Measurement analysis matrix.

Parameter	Data Matrix
Pushrod load (PR1 or PR3)	256 × 128
Torsional moment	256 × 128
Surface pressure (1 sensor)	2048 ×128
All pushrod (APR) loads	256 × (128*4)
AS1S surface pressure ($r/R = 0.200$)	(2048*19) ×128
AS1S Surface pressure ($r/R = 0.400$)	(2048*20) ×128
AS1S Surface pressure ($r/R = 0.675$)	(2048*18) ×128
AS1S Surface pressure ($r/R = 0.765$)	(2048*23) ×128
AS1S Surface pressure ($r/R = 0.865$)	(2048*25) ×128
AS1S Surface pressure ($r/R = 0.920$)	(2048*29) ×128
AS1S Surface pressure ($r/R = 0.965$)	(2048*25) ×128
AS1S Surface pressure ($r/R = 0.990$)	(2048*25) ×128
Sectional load c_m	2048 ×128
ASAS surface pressure	(2048 *184) ×128

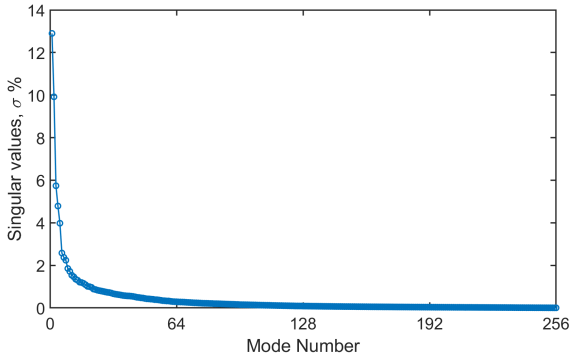

Figure 4. Singular values

are then assigned to their corresponding cluster. Assignment was achieved through curve fitting the time coefficients using a bimodal Gaussian mixture model (for a bimodal data) followed by probing the individual cycle on to the mixture model through the Gaussian probability method.

The last step in the clustering process is phase-averaging all the cycles that belong to a cluster to determine the cluster-average and variance. The process is repeated for each cluster. A byproduct from such analysis is the determination of group probability, i.e., percentage of occurrence of each cluster. Tables 2 shows the data matrix for all the choices of data analysis conducted in the present study. Data from the individual surface pressure sensors can be analyzed (1) independently, (2) by combining all the sensors at one radial station (AS1S), or (3) by combining all sensors from all stations (ASAS). An alternative to AS1S would be to use derived c_l, c_m, or c_d data that inherently use all the pressure sensors through integration. Both approaches have their own merits and shortcomings (Ref. 4).

Validation of Clustering Algorithm

The capability of NDC algorithm is first assessed to extract the similarities and differences among the blades (pushrod loads)

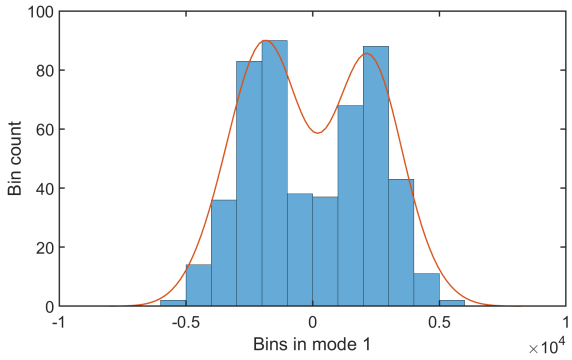

Figure 5. Histogram of pushrod loads using the first mode

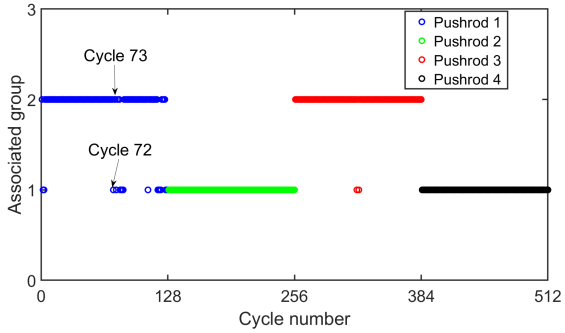

Figure 6. Cycles from all pushrods and the associated groups clustered using only the first mode

that were discussed earlier in the preliminary analysis. For this task, data from the fourth row of Table 2 was selected. Upon applying POD, a total of 256 spatial modes are generated and are sorted based on the singular values. Figure 4 shows the sorted singular value of each mode. To begin with, data analysis is first conducted using the first mode i.e., only the differences at the highest level are accounted for clustering in this step. More modes are included later. The resulting histogram of the time coefficients when using the first mode is shown in Fig. 5, which implies a bimodal data. The bin counts about zero in the x-axis suggests that the group sizes are almost even in that nearly equal number of cycles are present in each cluster. The cluster that contains negative bin values (in

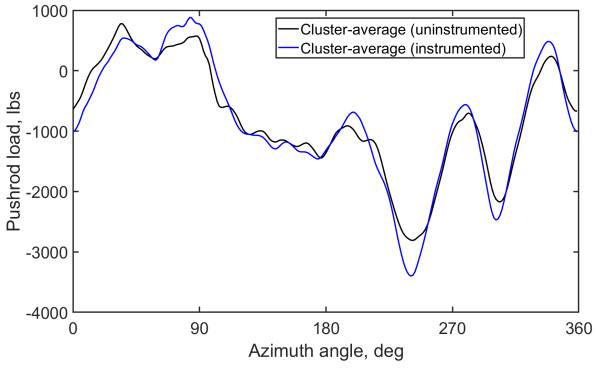

Figure 7. Cluster-averages of two groups present in the pushrod data

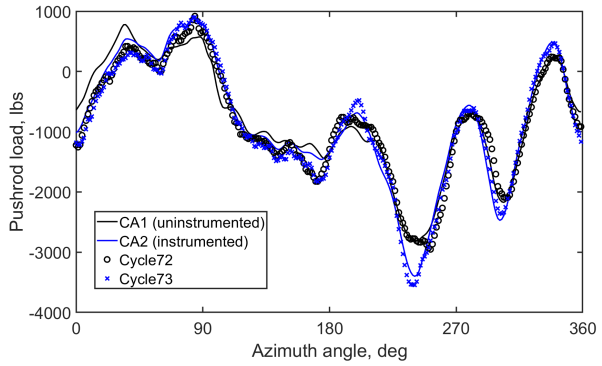

(a) Switched PR1 cycle

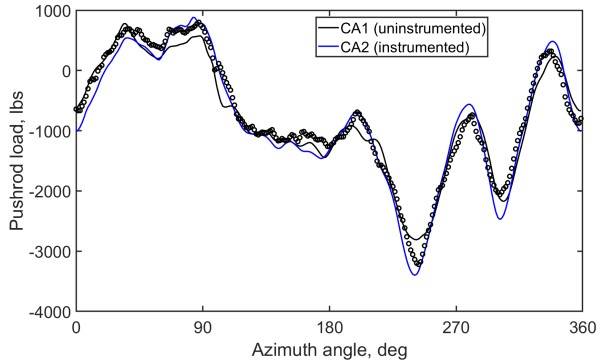

(b) Switched PR3 cycle

Figure 8. Explaining Cluster-averages using few individual cycles

the x-axis of the histogram) slightly outnumber the cluster on the right with positive bin values.

The identity of each cycle for each pushrod in terms of the group it belongs is shown in Fig. 6. The x-axis represents the cycle number and the y-axis represents the group number for each cycle. In the x-axis, each 128 cycles belong to one pushrod, i.e., cycles 1 to 128 belong to PR1, the second 128 (i.e., cycle numbers 129 to 256) belong to PR2 and so on as shown in the legend. The entirety of all the pushrod cycles connected to the un-instrumented blades (PR2 and PR4) belong to group 1. Among the pushrod cycles connected to the instrumented blades, a total of 18 cycles (16 from PR1 and 2 from PR3) were assigned to group 1, as well. The rest of the cycles in PR1 and PR3 formed group 2. The 18 cycles that switched groups from instrumented to un-instrumented blade cluster explain the slight bias seen in the histogram (Fig. 5). Cluster-averages for each group are then calculated by phase-averaging all the cycles present in a group and is shown in Fig. 7.

To understand the reason for certain cycles in PR1 (attached to the instrumented blade 1) to be assigned to group 1 that contains un-instrumented blades, two adjacent cycles from

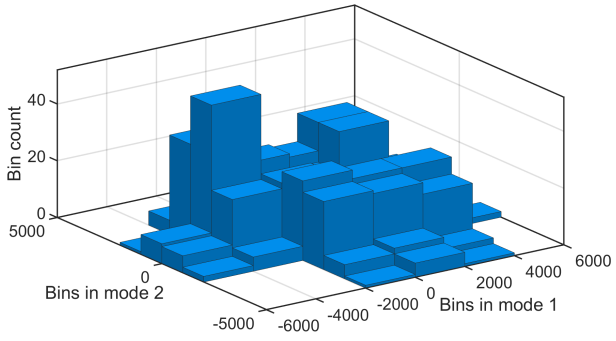

Figure 9. 2D histogram of time coefficients

PR1 (cycles 72 and 73) are plotted against the two cluster-averages in Fig. 8a. Cycle 72 switched to group 1 and cycle 73 stayed with majority of the PR1 cycles at group 2. The cluster-averages CA1 and CA2 are, as mentioned earlier, phase-averages of cycles contained in groups 1 and 2, respectively.

The un-switched cycle 73 follows CA2 throughout the azimuth explaining the reasoning behind the association (group 2). On the other hand, the switched cycle 72 follows CA2 only on the advancing side and then transitions to CA1 on the retreating side. Beginning from the wave form at 180° to the overall peak load at 240° azimuth (and the subsequent load peaks at 280°, 300°, and 330°), the correlation of cycle 72 with CA1 is excellent. With such good correlation (when combined with the higher magnitude of load seen on the retreating side) it is justifiable that cycle 72 belong to group 1 as assigned by the NDC algorithm; not with group 2 where the majority of PR1 cycles are assigned.

A similar depiction for one of the two switched cycles in PR3 is shown in Fig. 8b; In this case, the switched cycle follows CA1 between 0 and 45 degrees azimuth (against majority of the PR3 cycles that contributed to the formation of CA2 curve). Between 45 and 260 degrees (slightly past the overall-peak load azimuth), the switched cycle correlates well with CA2. However, after 260 degrees, the cycle correlates again well with CA1.

Comparing the characteristics of the switched cycles between the two instrumented blades, the reason for their assignment to the un-instrumented blade group 1 is different. Ideally, it may be desirable to create two more groups to account for the two different characteristics of the switched cycles. Assigning to one of the two groups, i.e., group 1 or group 2 is a limitation imposed by selecting only one mode; adding higher modes in the analysis would enable creating more groups to assign cycles appropriately. Figure 8, nevertheless, provides confidence on the algorithm that the groups selection is logical and can be explained with a reason.

To continue with the validation of NDC algorithm, clustering was conducted using two modes (as suggested by the singular values in Fig. 4). In this case, the input cycles were jumbled before decomposition as an added challenge. The 2D histogram of time coefficients is shown in Fig. 9. Four peaks

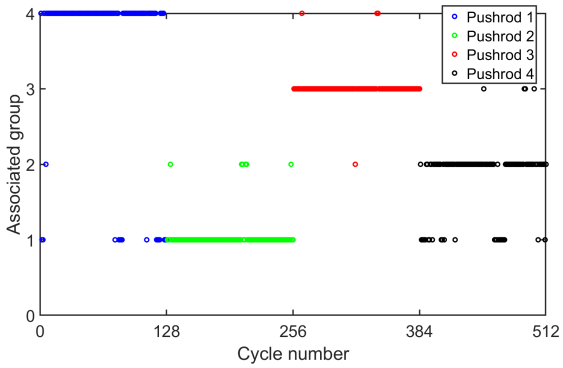

Figure 10. Cycles from all pushrods and the associated groups clustered using the first two modes

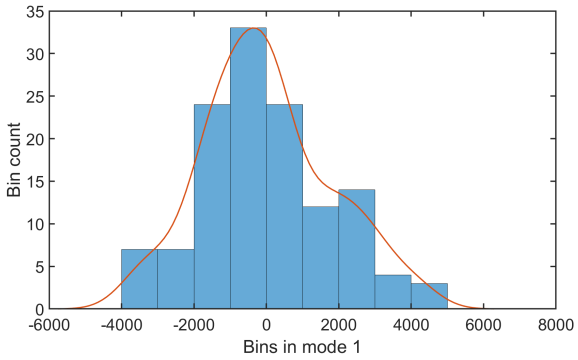

Figure 11. Histogram of time coefficients - R45P38 PR1

were detected which suggests the presence of four groups – an entirely expected outcome considering the rotor system uses four blades. Upon clustering as described earlier (Gaussian mixture model followed by probing each cycle) and resorting the cycles (as they were jumbled), the resulting cycle-group combination is shown in Fig. 10. Majority of the cycles that belong to each pushrod form their own group; by including a second mode with slightly lower energy, it became possible to separate the loads among all the four pushrods even though they were mixed together in the data analysis. The fundamental nature of the data, i.e., load cycles in each pushrod showing similar characteristics while differing with other pushrods, made such separation possible.

To summarize, when compared with the preliminary analysis discussed earlier, two groups of pushrod loads shown by NDC is consistent with the JPDF results (Fig. 3). The groups are a result of the structural property differences between the un-instrumented and the instrumented blade sets. The cluster-averages captured the differences between the two pushrod groups correctly, i.e., (1) the waveform difference near 180° azimuth and (2) the magnitude difference in the overall peak load (and the subsequent local peaks). When two modes were used, the algorithm separated the load cycles from all four pushrods successfully. Any cycle that was assigned to a different group from their majority counterparts was explainable. All the aforementioned results demonstrate the capability of the clustering algorithm.

Having verified the capability of the clustering algorithm, the next step is to analyze the individual pushrod loads and blade surface pressure to assess the presence of clusters. Computational validation is often conducted using one of the four blades (or pushrods) and the differences in the structural properties among blades are generally not accounted. A small change in the control system input, changes in the flapping characteristics, inadvertent trim tab changes, variations in the flow such as a strong/weak tip vortex from the previous blade could all have caused furcation in the data. Hypothetically, in the case of flight test, it could result from simple presence of gust as well. Separating these odd cycles from the rest of the cycles is essential to ensure that the acquired measurements were made at the desired operating condition and not inadvertently at other operating conditions.

RESULTS

In this section, beginning at the individual pushrod loads, clustering analysis is progressively extended to the blade surface pressure measurements made at all radial stations (sectional loads) and ended at the individual blade surface pressure sensor data. In the presence of clusters, correlation studies are conducted wherever possible among the aforementioned measurements to identify the radial sections and the associated aerodynamic phenomena contributing to the formation of pushrod load clusters.

From the all-pushrods (APR) data analysis, it was realized that a few cycles (such as cycle 72 on PR1) behaved differently compared to the majority of the cycles from the same pushrod. However, results from APR analysis alone are not sufficient to separate all the odd cycles in PR1. When data from all the pushrods are used in POD, the identified basis inherently attempts to maximize the pushrod-to-pushrod load differences, i.e., not within a given pushrod. The mode shapes are arrived in such a way that minimum number of modes are needed to reconstruct the most common azimuthal variations in the data set. In the case of 4-bladed rotor system, the mode shapes are chosen optimally to allow reconstruction of the azimuthal load variations of all pushrod loads. Forcing cycles to choose one of the top four characteristics found in a 4-bladed set does not allow separating more variations that may occur within the blade. Instead, decomposition of a smaller subset of data, i.e., measurements using one pushrod maximizes the load differences found within the pushrod.

PR1 is chosen for conducting the clustering analysis on individual pushrod loads as it allows correlation studies against the surface pressure measurements made on blade 1. For reference, X in Eq. 1 in this case is a 256×128 data matrix as given in the first row of Table 2.

PR1 Load Analysis

Histogram of the time coefficients obtained using the first mode for the PR1-only cycles (case R45P38) is shown in Fig. 11. Two peaks can be seen, meaning two groups are

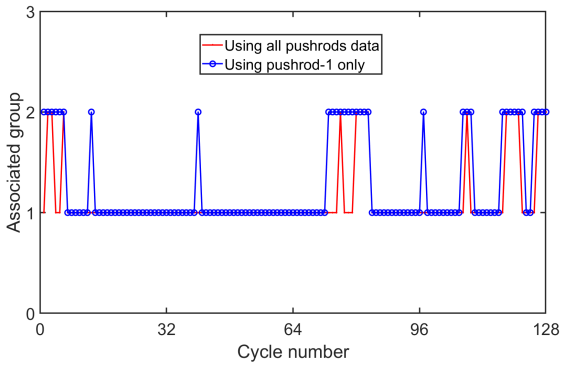

Figure 12. Comparison of PR1 clusters when grouped using APR and PR1-only data sets - R45P38)

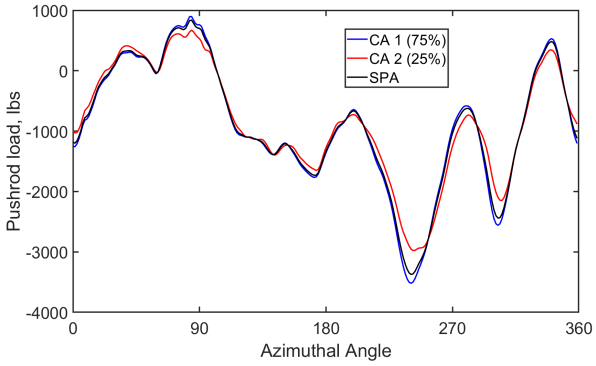

Figure 13. Cluster averages of PR1 loads R45P38

present even within the PR1 data. Clustered cycle-group combination is shown in Fig. 12 along with results from all-pushrods data analysis for comparison. Bimodality within PR1 data is not unexpected considering 16 cycles from PR1 switched groups in the APR data analysis.

The two clusters are unequal in size, as conveyed by the histogram (Fig. 11). The groups had a ratio of 75% to 25% ratio, i.e., 95 cycles (out of 128) formed group 1 and the remaining 33 cycles formed group 2. Compared to the 16 switched PR1 cycles found during the APR data analysis, the size of group 2 cycles increased, as expected. All the aforementioned 16 cycles are part of a similar but larger group 2 with 33 cycles.

The cluster-averages from analyzing PR1-only data is shown in Fig. 13. Detailed visualization of the clustered results is shown in Fig. 14 that includes cluster-averages of the two groups, conventional SPA, and all the cycles that constitute groups 1 and 2 (color coded). SPA lies between the two cluster-averages at all the azimuths, and is closer to the CA1 because of the higher number of cycles found in group 1 compared to group 2. The constituent cycles of each group are scattered around their corresponding cluster-averages. Clustered cycles show similar behavior, as expected. For example, all the group 1 cycles that showed higher peak load compared to the group 2 cycles at 240° azimuth stayed together showing higher load than group 2 at subsequent azimuths, i,e, at 300° and 330° as well.

Tables 3 and 4 provide statistical details of the clusters. Data

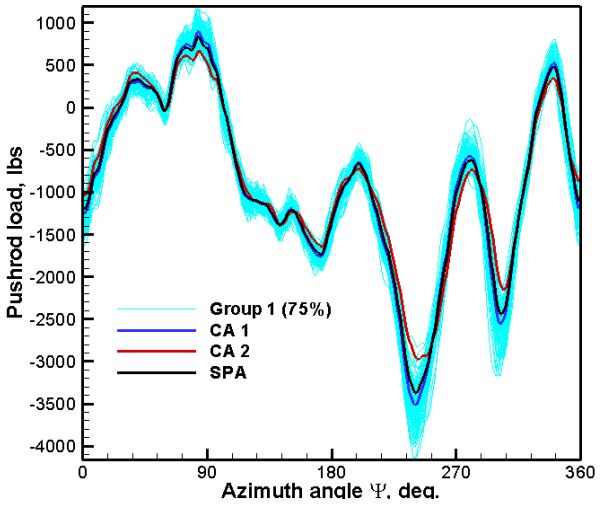

(a) Group 1 cycles and Cluster 1 average

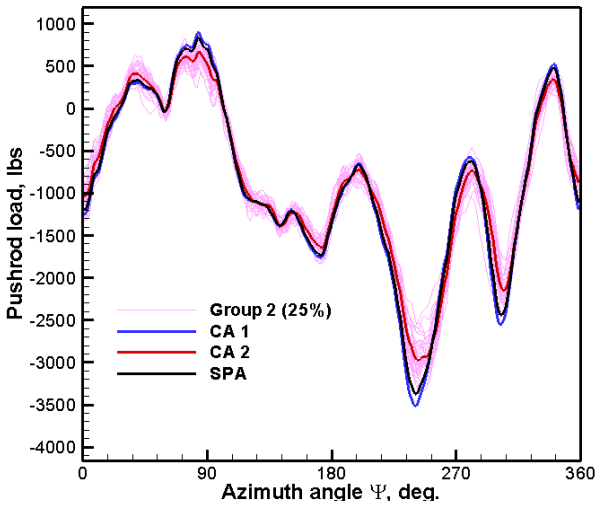

(b) Group 2 cycles and Cluster 2 average

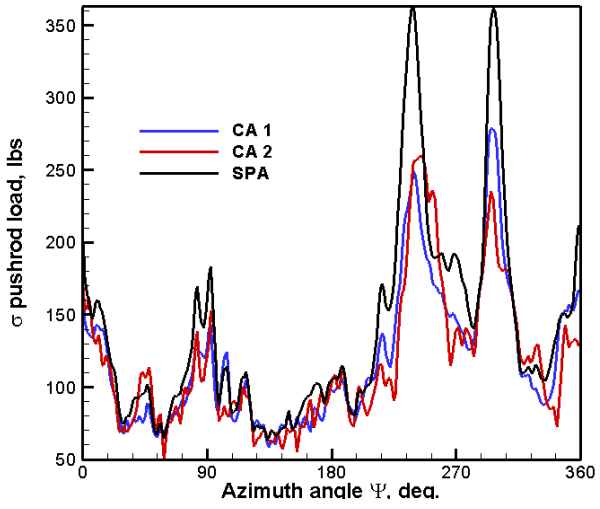

(c) Comparing the standard deviation

Figure 14. Results of clustering R45P38 PR1 data

in Table 3 is obtained from the cluster- and the phase-averaged curves and Table 4 is obtained from the individual cycles.

From the peak load perspective, CA1 is at least 550 lbs higher than CA2. In other words, conventional SPA incorrectly combines two groups that differ by 18% at peak load. Compared to the conventional SPA, the peak loads of CA1 and CA2 are about 5% higher and 12% lower than the SPA, respectively. The lower peak load from group 2 may not carry significance in designing pushrods, however, a 5% higher peak load obtained from 75% of cycles is important. From CFD validation perspective, however, both results have significance.

Figure. 14c shows that the standard deviation is reduced across all azimuths for both the clusters compared to SPA. Such result confirms that the cycles within the two groups are relatively similar, however, the two groups are different from each other. At the peak load, the standard deviations of both CA1 and CA2 are lower than the SPA by about 30%, i.e. σ reduced from 10.5% to about 7% of the peak load. Reduced standard deviation, when combined CA1 load characteristics, not only suggest that the pushrods are experiencing higher peak load, but also with more certainty compared to the conventional SPA approach.

Description	SPA	CA1	CA2
Mean peak load (lbs)	-3373.5	-3523.6	-2968.4
σ at peak load (lbs)	351.45	245.18	238.05
Peak load azimuth (deg)	240.46	240.47	241.88

Table 3. Cluster- and phase-average curve statistics

Description	All cycles	Group1	Group 2
No. of cycles used	128	95	33
Ave. peak load (lbs)	-3411.2	-3547.5	-3018.9
σ at peak load (lbs)	330.80	242.74	217.64
Ave. ψ at peak load (deg)	241.64	240.44	245.11
$\sigma\psi$ at peak load (deg)	3.175	1.5	4.08

Table 4. Statistics obtained using individual cycles

Considering the historical significance of using SPA, recommendations for any alternative (in the presence of clusters) must be met with rigorous analysis to ascertain the improved representation of the data. In the present study, such a requirement means (1) conclusively demonstrating the presence of clusters, and (2) ensuring cluster-averages are good representations of the cycle-to-cycle (and cluster-to-cluster) variations found in the data. While the former requirement is one of the key objectives of the present work, the following discussion attempts to answer the latter requirement.

Comparing Tables 3 and 4 provides insight about data distribution within the clusters. For example, the peak loads obtained from CA1 curve (3523.6 lbs) and the average of peak loads obtained from group 1 cycles (3547 lbs) are within 1%. The standard deviation is nearly identical as well (242.74 vs. 245.18). The azimuthal position where peak load occurs is also nearly identical between the individual cycle statistics and the CA1 (240.44 vs. 240.45 deg.), which suggests CA1 represents group 1 accurately.

It should be understood that even the cluster-averages are obtained by phase-averaging all the cycles in a given group. As a result, any aperiodic variation in the peak load azimuth would not only smear the peak load magnitude but also the azimuth when the peak occurred. The reason for such a good agreement between CA1 and group 1 cycle statistics suggest that the characteristics of the cycles within the cluster are nearly periodic in terms of the load and the azimuthal occurrence. The variation in the peak load azimuth (σ_p) for group 1 cycles is 1.5 degrees (half of SPA).

Group 2 is not as compact as group 1. The difference in the peak load (CA2 peak vs. average of the individual cycles in group 2) is about the same as SPA (and higher than the group 1 statistics). Also, the difference in the peak load azimuth between CA2 and the average of group 2 cycles is high (241.88° vs. 245.11°, i.e., about 4 degrees), along with the scatter magnitude ($\sigma\psi_p$). In essence, group 2 cycles are characterized by large azimuthal variations in the occurrence of peak load, which translates into higher scatter in loads because of high gradients in loads ($d\ load/d\psi$).

One of the key differences between the group 1 and group 2 cycles is the peak load azimuth (240 vs 245 deg., respectively). Conventional SPA simply combines the two groups with different peak loads (that occur at different azimuths) resulting in higher scatter while determining pushrod loads. In other words, SPA represents a bimodal distribution using normal distribution parameters.

Other Test Cases

No clusters were found in both the lower thrust cases (R45P35 and R45P36). Consequently, SPA can be confidently applied to represent the load variations. However, PR1 loads of R45P37 (with nearly the same thrust as R45P38 and slightly different control inputs) showed bimodal distribution. The clustered loads are shown in Fig. 15. The difference in the cluster-average peak loads for the two groups is about 1000 lbs (i.e., 3752 lbs vs. 2793lbs), even higher than the R45P38 that showed 550 lbs. There are some interesting similarities and differences comparing the two test points that produced clusters. The similarities include: (1) large differences in the peak load between the two CA(s) , (2) SPA aligning closer with CA1 because group 1 is larger in size compared to group 2, (3) a compact set of group 1 cycles with reduced load variations (σ) compared to group 2 , and (4) separating the smaller group 2 cycles reduces the load variations (σ) for the larger group substantially compared to the conventional SPA analysis (about 30% reduction at peak load and at subsequent high load azimuths), and (5) groups stay together at all azimuths, i.e., a group that exhibits higher load at one azimuth compared to the other group continue to show higher loads at subsequent azimuths.

It was argued in R45P38 that group 2 cycles carry less significance in pushrod design because they show lower loads than

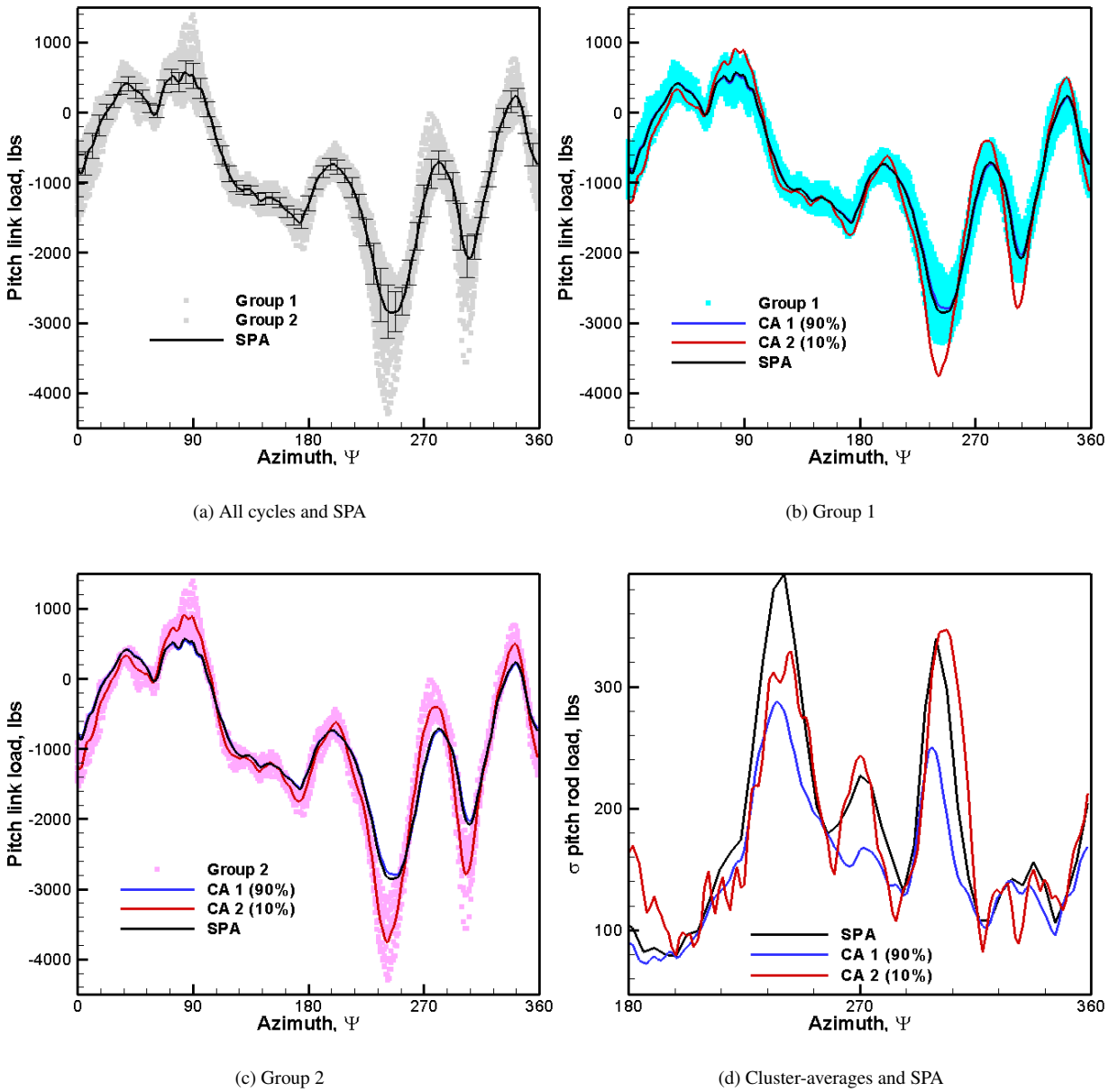

(a) All cycles and SPA

(b) Group 1

(c) Group 2

(d) Cluster-averages and SPA

Figure 15. Cluster analysis of R45P37 PR1 data

group 1 cycles (and SPA). However, in R45P37, it was the smaller group 2 that produced 30% higher load than group 1 cycles on average (and SPA). Nearly 10% of the cycles showing consistently higher loads is an important outcome of the clustering analysis that must be accounted for during pushrod design process. Another observation from the two cases is that the group that stalls earlier always produces higher loads (group 1 for R45P38 and group 2 for R45P37).

To summarize, clustering analysis on pushrod loads showed no groups in the lower thrust cases (i.e., normal distribution) and two groups in both the higher thrust cases. NDC algorithm successfully separated the two groups; the peak loads between the two groups differed by 550 lbs and 1000 lbs in R45P38 and R45P37 test points, respectively. In other words, conventional SPA incorrectly combined two groups of loads that were separated by an average peak pushrod load differences of 25%. Consistently, at least one group produced higher peak load than when using SPA. Clustering reduced the standard deviation of both the clusters compared to the all-cycle SPA analysis, which suggests cluster-averages provide better representation of the variations found in the pushrod loads.

While the clustered results exhibit the importance of representing a bimodal data accurately, as mentioned earlier, more effort should be taken to unambiguously ascertain the presence of clusters by other means before recommending cluster-averages *in lieu* of SPA. The next step provides a different path through correlation using another measurement, i.e.,

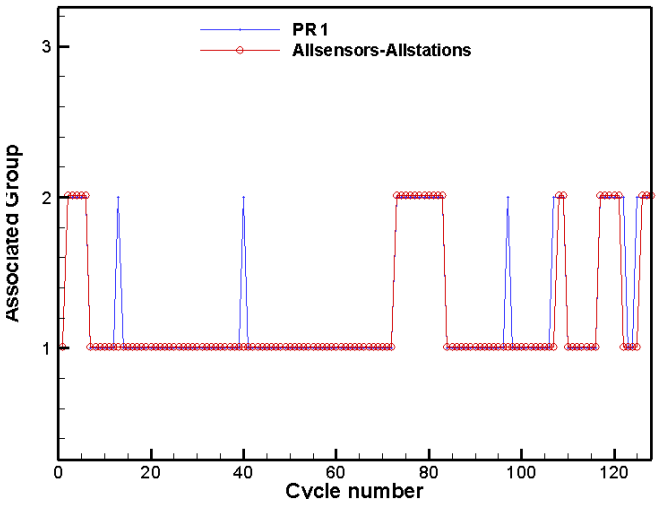

Figure 16. Comparing the clusters between pushrod and surface pressure sensor data (R45P38)

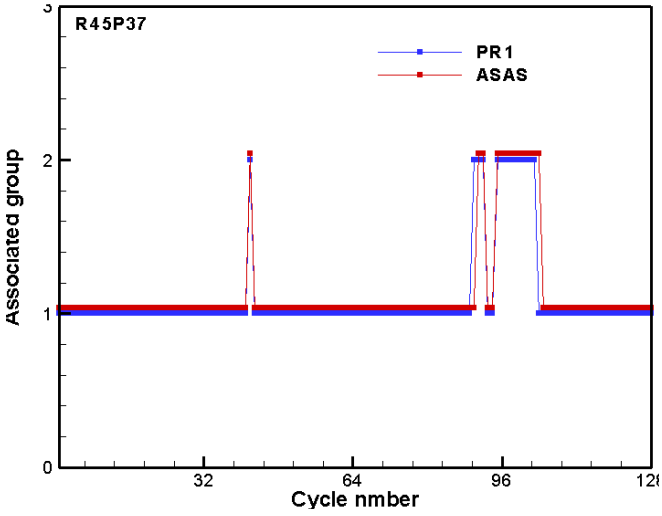

Figure 17. Comparing the clusters between pushrod and surface pressure sensor data (P45R37)

blade surface pressure.

Relating Pushrod Loads and Blade Surface Pressure

The azimuthal load variations of pushrods represent the aerodynamic environment experienced by the blades, at least partly. As mentioned earlier, load fluctuations are caused by the interaction between the rotor blades and the tip vortices trailing from the other blades. Dynamic stall and subsequent aeroelasticity induced load changes at various blade sections also affect pushrod loads. Results from the clustering analysis using the all PR data showed that some cycles experience different aerodynamic environment than the others. The following section attempts to understand the source for such clustering by analyzing the airloads through blade surface pressure measured using transducers mounted on the rotor blades. Any further reference to pushrod data represent PR1-only analysis unless specified.

To conduct this analysis, data from all the surface pressure transducers at all the radial stations (last row in Table 2) are used. This is a large data set comprising of 128 cycles of data acquired at 2048 per revolution over 184 surface pressure sensors that are distributed over 8 radial stations. The data is concatenated to a matrix (X in Eq. 1) of (2048x184) $\times$ (128). The data set is referred to as all-sensors at all-stations (ASAS).

Upon applying NDC algorithm, ASAS also produced two clusters for both the higher thrust cases. The cycle-group combination for R45P38 and R45P37 are shown in Figs. 16 and 17, respectively. In both cases, ASAS based clustering shows fewer group 2 cycles than the PR1 based clustering. In the case of R45P38, 25 cycles were found in group2 as opposed to the 33 cycles in the PR1 analysis. The difference in the number of cycles is not unexpected; pushrod load is an integrated effect over the entire blade surface while the ASAS data is acquired at 8 discrete radial stations. Also, equal weight given to all the sensors at all the radial stations in the POD analysis may have played a role in diluting the contribution of some cycles at some stations. Conducting clustering analysis at individual radial stations may provide the answer along with an improved understanding of the clusters.

Nevertheless, Figs. 16 and 17 show remarkable correlation between two completely different measurements (PR loads measured using strain gauges at 256/rev and ASAS surface pressure measured across the entire blade span using 184 pressure sensors at 2048/rev) for two different test points. These cases suggest that (1) blades are experiencing two different flow conditions for a given control input, and (2) airloads are the primary cause for data clusters found in pushrod loads. The next step is to identify the specific radial stations that may have contributed to the formation of clusters in the ASAS and PR1 data sets.

Clusters At Radial Stations

As mentioned earlier, not all radial stations produce strong loads that translate into higher pushrod loads. However, identifying those radial stations with high sectional loads is of interest for rotor blade design. Furthermore, computational simulations stand to benefit from such analysis as validation at multiple radial stations using data with improved accuracy becomes possible (Refs. 19–22). This section discusses the results from conducting NDC analysis on the surface pressure measurements made at several individual radial stations. The data set and the results will be referred to as all-sensors at one station (AS1S). Results are discussed in detail for the R45P38 cases; other test point are compared and contrasted for brevity.

The data set correspond to rows 5 through 12 in Table 2. These are not individual surface pressure sensor data rather a collection of all the sensors located at a given radial station. For example, at 67.5% station, the data matrix (X in Eq. 1) is (2048x18) $\times$ 128, where 2048x18 rows correspond to the 18 sensor data concatenated over 2048 data points per revolution and 128 represents the number of cycles. Out of the 8 radial stations, the two inboard stations (20% and 40%) and the outmost station (99%) did not show any clusters at least for R45P38.

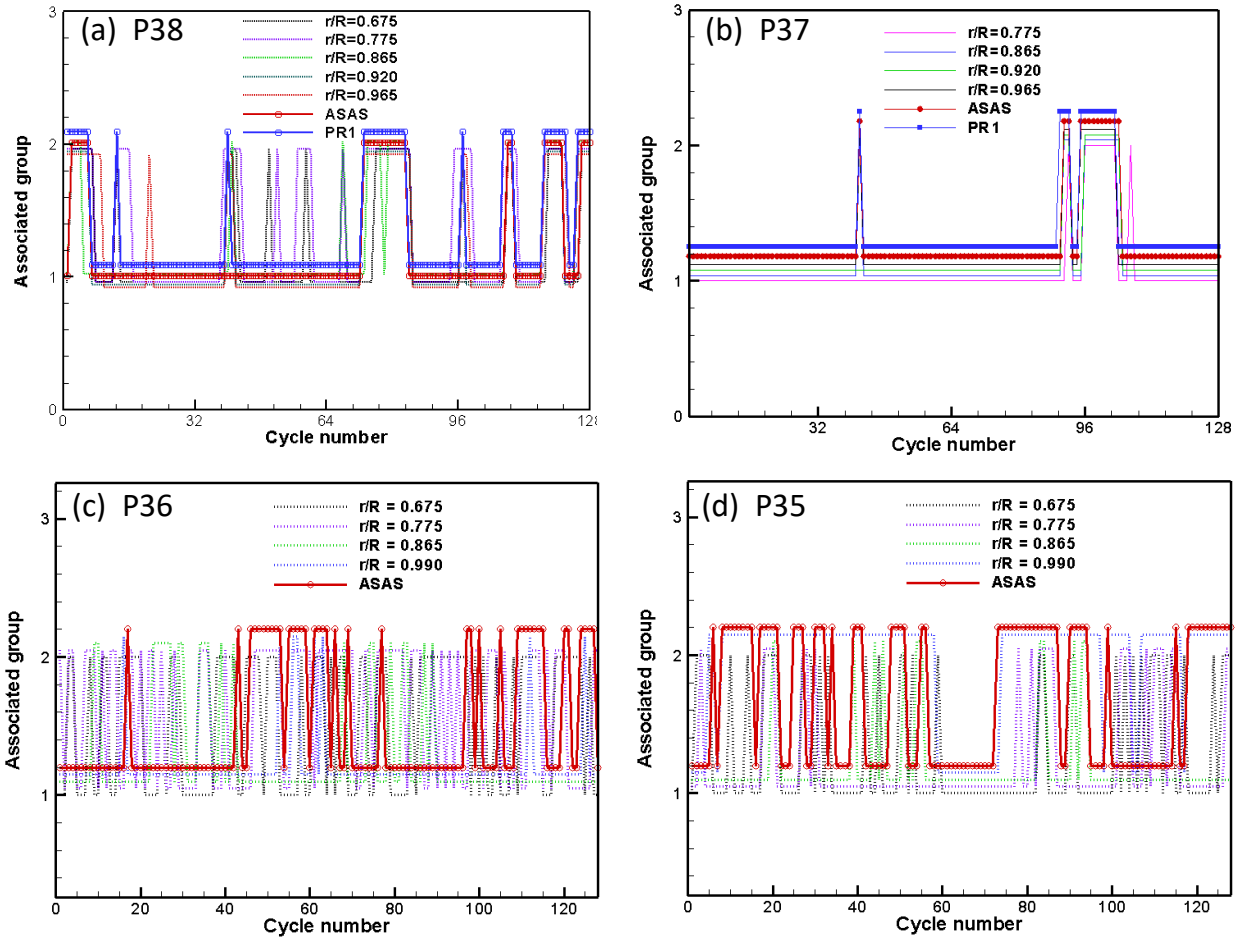

Figure 18. Comparing clustering results using different data sets for all cases

For the radial stations that produced clusters, beginning from 67.5% up to 96.5%, the results are shown in Fig. 18 along with ASAS and PR1 clusters. Different radial stations produce different clusters; the aerodynamic environment varies along the blade. Assessing Fig. 18a that correspond to R45P38, the source for the ASAS and PR1 clusters can be understood. PR1 cycles are assigned to group 2 when cycles from one or more radial stations were assigned to group 2. This figure explains the missing 8 cycles, i.e., 25 vs. 33 group 2 cycles found between ASAS and PR1 cases, respectively as shown in Fig. 16. Those additional 8 cycles found in PR1 came from several individual radial stations, whose load contributions (as felt physically by the pushrod) were diluted mathematically in the ASAS analysis due to the equal weight given to all the stations. Figure. 18 corresponds to R45P37 case; the results are similar to the R45P38 case however the clusters across the radial stations are more synchronous.

Figures 18c and d correspond to lower thrust cases R45P36 and R45P35, respectively. Even though distinct clusters exist at several radial stations and are relatively synchronized enough to cause ASAS clustering, pushrod loads exhibited normal distribution in the data. This may be because the loads are not large enough to translate into pushrod load variations. However, they are mathematically significant to produce clusters in ASAS analysis. Results from the two lower thrust cases emphasizes the significance of the two higher thrust case results, where loads are large and synchronized enough to be seen in both ASAS and pushrod clusters.

Cycle vs. group-number plots (shown in Fig. 18) helped identify the radial stations that contribute to the pushrod load clusters. The next step is to plot the sectional loads at the corresponding radial stations to assess the magnitude of difference between the clusters.

Sectional Loads Figure 19 shows the azimuthal load variation of clustered M^2 c_m at 67.5% radial station for all the test points. Predictions made using Helios are plotted alongside (wherever needed) to take advantage of its capability to provide flow field information that can explain the aerodynamic phenomena causing clusters. Details related to Helios implementation are provided in Refs. 22, 25–27. Four important azimuthal snapshots of flow field are shown in Fig. 20. Each azimuth has two perspectives: (1) a view from above the rotor plane and (2) an $r-z$ plane taken 1-inch in front of the blade. The latter moves with the blade and allows visualizing the aerodynamic features such as the tip vortex and the trim

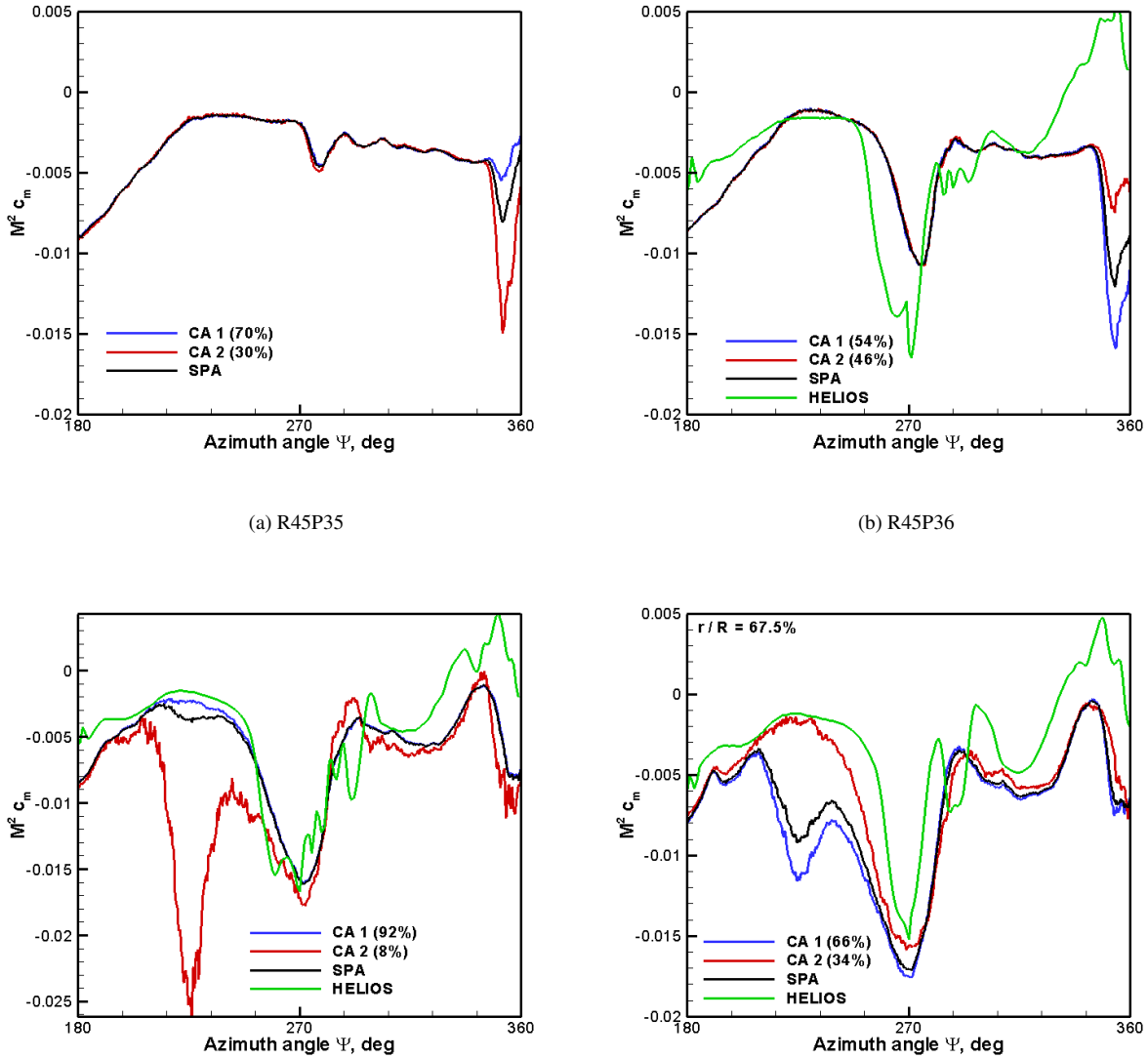

(a) R45P35

(b) R45P36

(c) R45P37

(d) R45P38

Figure 19. Representative summary of clustered data at 67.5% radial station for all test cases

tab vortex that the blade is about to interact. The top view plots are made using isosurface of Q-criterion and the colors represent vertical velocity. Red represents upward flow and blue represents downward flow. For example, separation can be noticed using red shades on blades (see Fig.20a for flow separation near the root section). The lower $r-z$ plane has vorticity as the color contour to highlight the tip and trim tab vortices.

At r/R=67.5%, Fig. 19 shows three key azimuths: 225°, 270°, and about 345°. Observations from the three azimuths are discussed in detail.

At 225° azimuth: There are no clusters at 225° azimuth for the lower thrust cases. However, both the higher thrust cases display similar kind of clusters. One group shows stall that is accompanied by high moment magnitudes while the other group is free of stall. For R45P37, about 8% of the 128 acquired cycles (group 2) show deep stall. The cluster-average (CA2) was higher than the highest value represented using SPA at 270°. The larger sized group 1 cycles (92% occurrence), on the other hand, did not stall. The group proportion (8% and 92%) is very similar to the pushrod load groups for R45P37 shown in Fig. 15, suggesting that the 67.5% station plays a big role in the pushrod load clusters. Interestingly, it is the smaller group that produces higher loads in both the PR1 loads and at the 67.5% radial station. More importantly, SPA did not show any semblance of stall, obscuring the effect of 8% of cycles that cause significant moment (and PR loads).

In the case of R45P38, group 1 and 2 switched their charac-

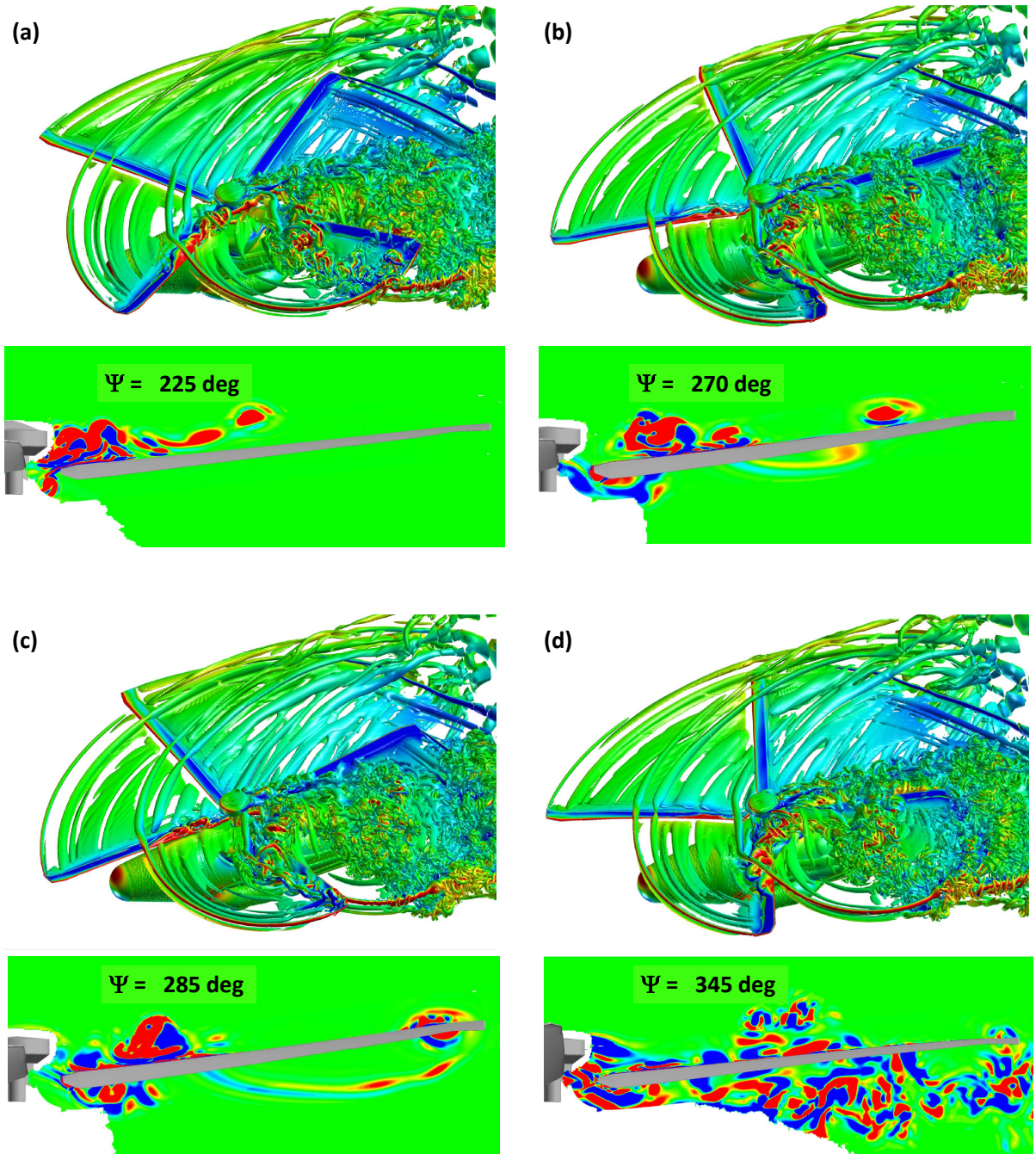

Figure 20. Simulated flow field at various azimuths (R45P38)

teristics compared to R45P37, however, showed similar excellent correlation with pushrod load clusters in both group proportion and in load characteristics. Larger group (66%) stalled and the smaller group (34%) showed no signs of stall, which matched the higher pushrod loads for the larger group 1 (Fig. 14b and lower loads for the smaller group 2 (Fig. 14c). Even though both test points (R45P37 and R45P38) were conducted at the same thrust conditions, the small difference in the control inputs (and the resulting flapping response of the blades) may have played a role in the observed differences.

At 270° azimuth: There is a gradual increase in the severity of stall as thrust increases (i.e., from R45P35 to R45P38). Clusters are seen only at higher thrust conditions albeit with smaller difference in peak load magnitude between the clusters compared to 225° azimuth.

Helios predictions followed the no-stall group at the 67.5% station for both the test points (R45P37 and R45P38). Predictions at R45P38 deserve more attention because the conven-

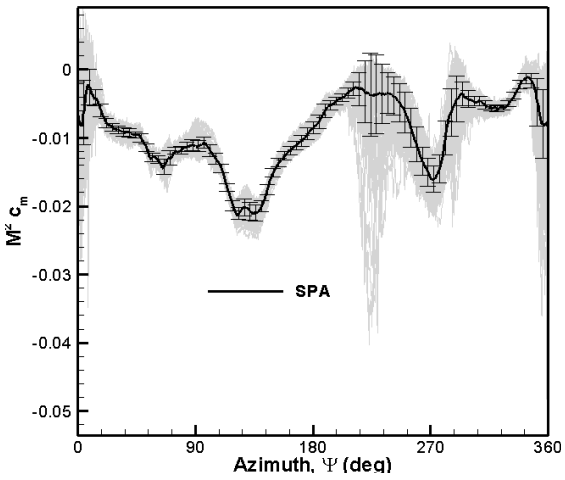

(a) All cycles and SPA

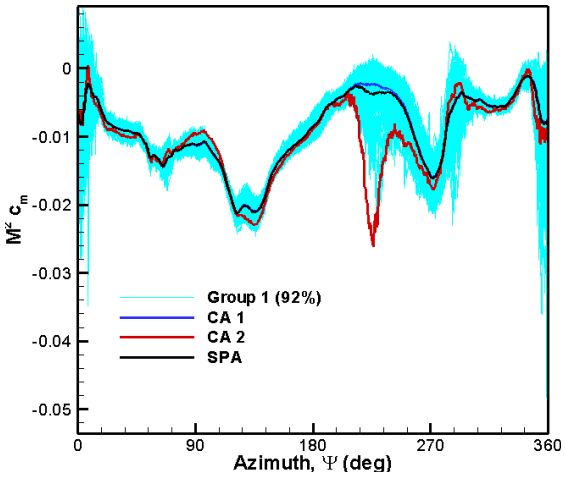

(b) Group 1 cycles

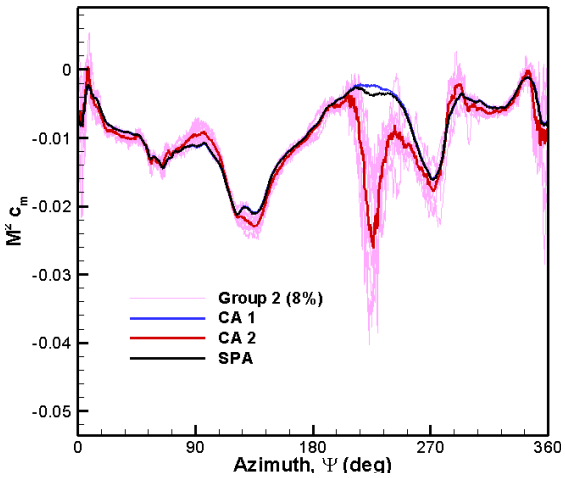

(c) Group 2 cycles

Figure 21. Cluster analysis at r/R=67.5% radial station for P45R37

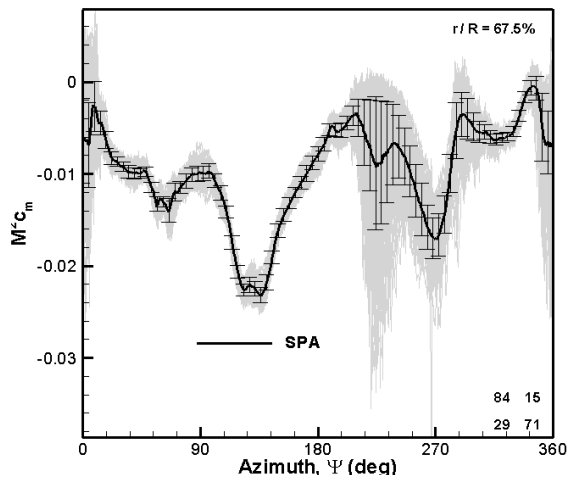

(a) All cycles and SPA

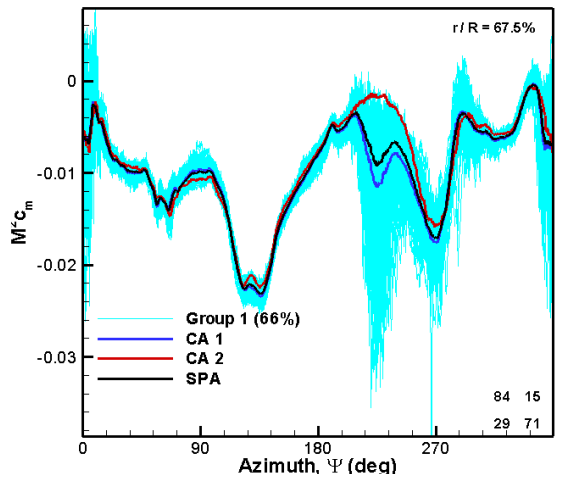

(b) Group 1 cycles

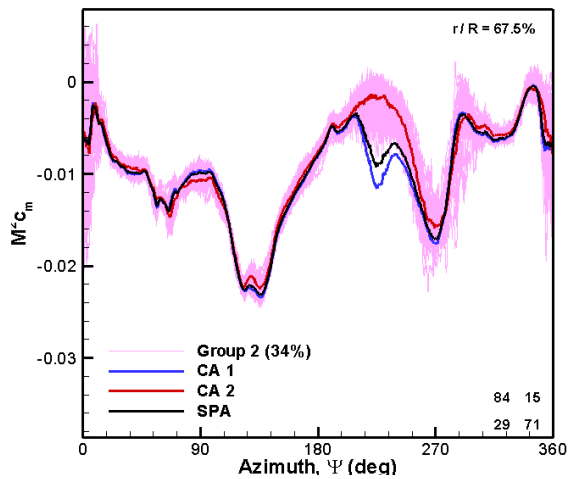

(c) Group 2 cycles

Figure 22. Cluster analysis at r/R=67.5% radial station for P45R38

tional SPA suggests the presence of stall (even though 34% of the cycles did not exhibit stall). Not only did Helios show better matching with the no-stall group 2 at 225° azimuth, it continues to show good correlation with the group 2 c_m peak at 270° as well. This can be related to behavior of cycles within a group seen earlier, i.e., all cycles within a group tend behave in a similar way at multiple azimuths.

Taking into account the improved correlation between Helios and group 2 cycles (compared to SPA) at higher thrust conditions, predictions can be used to visualize group 2 flow field, as experienced by the blades. Figure 20b $r-z$ plane view (corresponding to R45P38) suggests that the stall at 270° azimuth is caused by the blade interaction with the trim tab vortex. While blade tip vortices present in the rotor wake are known to trigger stall (Refs. 23, 24), the deformed trim tab vortex (with reduced vorticity magnitude compared to 225° azimuth) appears to indicate interaction with the blade resulting in stall. Even though tip vortex shows close proximity and its induced velocity may play a role in the stall, the interaction between tip vortex and blade occurs later at 285° near 86.5% radial station, as shown in Fig. 20c. Both the trim tab vortex and the tip vortex are from the preceding blade. With the interpretation that the stall causing mechanism may be the trim-tab vortex, the severity differences in the peak c_m magnitude between the two clusters at 270° came either from (1) the aeroelastic response to stall at 225° azimuth or (2) from the aperiodicity in the strength and spatial location of the trim tab and/or adjacent tip vortex (Ref. 10).

Even though the predictions did not capture the higher occurrence group (i.e., group 1 with 66% occurrence), correlating significantly better with group 2 results at multiple azimuths (compared to SPA) provides added confidence to the predictive accuracy of the simulations. Such correlation allows newer questions to arise, such as identifying methodologies to capture the observed stall at 225° seen in group 1.

At 345° azimuth: Both the lower thrust cases show the presence of two clusters. Consistent with the 225° azimuth, one of the clusters showed no stall or light stall and the other showed deep stall. Higher thrust cases showed no clusters. Even though there are two curves at 345° for the higher thrust cases, their values are relatively close to each other. Therefore the source for the formation of clusters may not have come at that azimuth. Helios predictions are significantly different from either of the groups found in the lower thrust measurements. Consequently, flow field predictions may not be useful. However, the trend and magnitude are relatively close to R45P38 measurements allowing predictions to visualize the flow field (Fig. 20d). The blade at 67.5% station appears to be engulfed by the turbulent wake comprising of hub wake, tip vortex, trim tab vortex, stalled and separated flow from the retreating blade etc. While significant scatter may be expected in such flow field, no clear clusters can form as shown by the measurements and predictions.

Detailed visualization of the clustered results for both the higher thrust cases R45P37 and R45P38 at 67.5% radial station are shown in Figs. 21 and 22, respectively. The color coded cycles plotted against the cluster-averages show the repetitiveness within each group, the difference between the groups, and the improved representation of the groups using cluster-averages compared to the SPA.

Chordwise c_p Distribution: Sectional load clusters quantified the difference between the two groups. And, Helios helped visualizing the flow experienced by one of the two groups and possible sources of furcation in loads. To complement Helios and to conclusively ascertain the existence of two different flow conditions (as experienced by the blades), time-stamped, chordwise c_p distribution covering one full-rotation of the rotor was plotted at 67.5% radial station for R45P37 in Fig. 23. The two solid lines represent the cluster-averages resulting from applying the NDC clustering algorithm on all the blade surface pressure sensor data (AS1S) at 67.5% station. Blue and red colors are chosen to match the unstalled and stalled groups found in the sectional moment clusters shown in Fig. 21, respectively. Along with the cluster-averages, one individual cycle from each group is plotted through blue and red circles for each sensor. The subjectively selected individual cycle represents the extreme case in each group. The following discussion is based on the cluster-averages, however, the individual cycles can be seen to exaggerate all the observations made from the cluster-averages.

From 0° to 202° (slightly into the retreating side), both groups exhibit similar variation. The general characteristics include increase in the suction pressure (80°), the suction and the pressure sides switching roles near the leading edge at 122° etc. As expected, chordwise c_p distribution showed the difference at 217° and 226° azimuths. While the blue group continues to remain attached, red line stalled. The individual cycle showed separation until 60% chord at 217° that extended up to the trailing edge at 226°. At 277° both groups became similar again and remained until the end of the revolution. Considering the difference seen between the two groups, it can be conclusively stated that two different flow conditions exist and that the SPA incorrectly combines the two conditions into one data set.

Similar results are found at several other radial stations, however, further discussion is limited to the 86.5% radial station for R45P37 test case as it shows interesting correlation with Helios – see Fig. 24). The stall at 285° is a result of the interaction between the tip vortex and the rotor blade. Clusters in this case are a result of bimodal data distribution at 345° azimuth; the peak c_m magnitude between the two clusters differs by about 38%. While CA1 shows M^2 c_m of 0.29, CA2 and SPA show about 0.21. The two groups are almost equal in size. Figure 25 shows CA, SPA, and all the individual cycles color coded based on the associated group. SPA appears to be a good representation of the scattered data in Fig. 25a. However, upon clustering, the shortcoming of SPA becomes clear.

There are two groups of data that are differentiated by the peak load azimuth and the peak magnitude of moment. As mentioned earlier in the pushrod load analysis, SPA suffers from the scatter in the azimuthal occurrence of peak c_m mag-

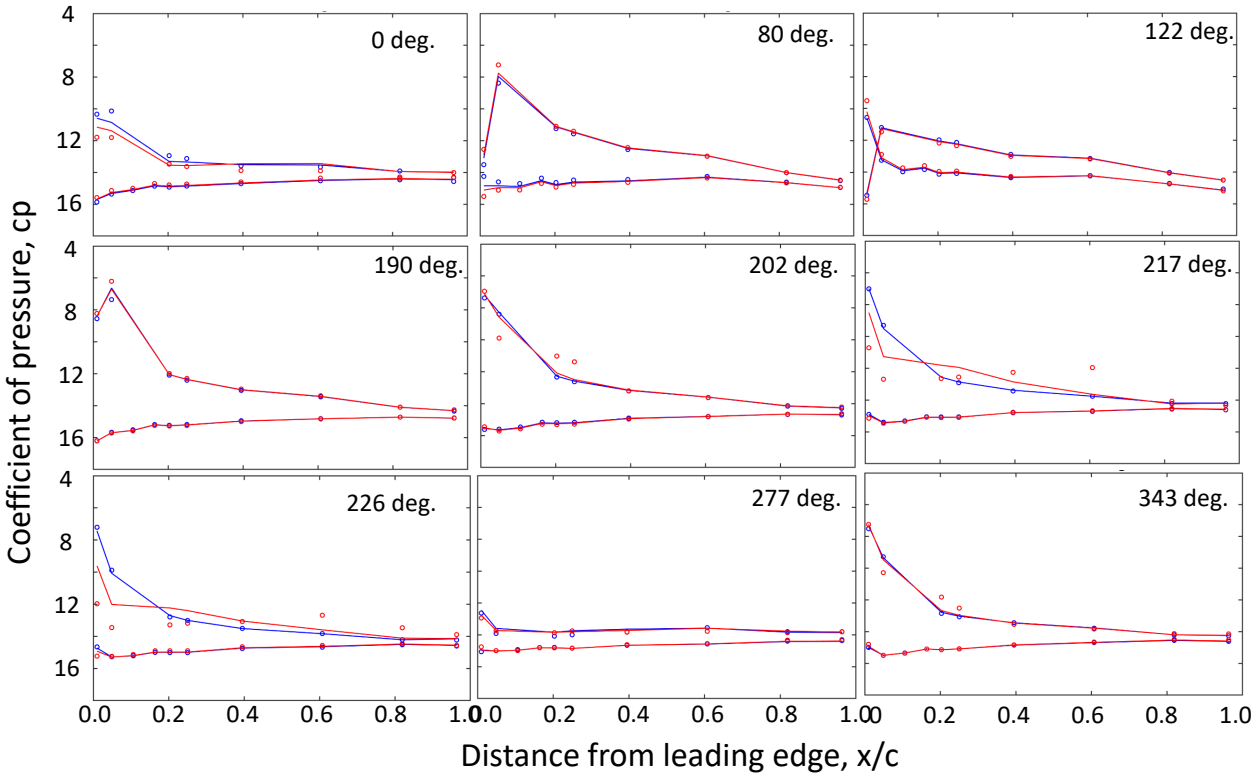

Figure 23. R45P37 - clustered c_p distribution at 67.5% radial station (solid lines: cluster-averages, circles: one individual cycle from each cluster).

nitude that translates into incorrect determination of peak sectional loads (along with high scatter). Clustering the data represents the groups appropriately and reduces scatter in both the groups compared to SPA. A close up view of standard deviation is shown in Fig. 25c.

Figure 24 shows Helios over-predicting peak c_m when compared with SPA at 345° azimuth. Also, stall was believed to have occurred earlier than measurements. Clustering results show that there exists at least 50% of cycles matching the predictions of Helios both in terms of peak magnitude and azimuthal occurrence, adding more confidence to the predictive capability of Helios. Flow field corresponding to this azimuth can be seen in Fig. 20d. While other radial stations are engulfed by turbulent wake, the 86.5% station seems to be free of such turbulence. Time stamped chordwise distribution of c_p at 340° azimuth is shown in Fig. 26 to understand the flow distribution on the blade surface. The red group shows separation from the leading edge to about 60% chord and the blue group shows separation only until 30% chord. The difference in the separation location contributed to the difference in the sectional moment as seen in Fig. 24. It appears there are two sources for the formation of clusters at 86.5% station: (1) chordwise location of separation and (2) peak load azimuth. Nevertheless, consistent with the 67.5% station, c_p distribution further confirms the presence of clusters through two clearly distinct flow conditions experienced by the blade.

Individual Blade Surface Pressure Sensor

To complete the clustering analysis that began at the pushrod loads that was followed by ASAS, AS1S, and sectional moments, similar analysis was conducted at the smallest subcomponent in the measurements, i.e., individual blade surface pressure data. Again, POD was conducted using Eq. 1 with X representing 128 cycles of blade surface pressure measured at 2048Hz. A representative result from applying NDC algorithm at one radial station (67.5%) and one chordwise station (1/4th chord) for R45P38 is shown in Fig. 27. Results from applying JPDF are shown as well for understanding the data distribution. Again, two groups of data can be seen. One group showed stall and the other showed no separation. The group proportion (75% vs 25% for group 1 and 2) is consistent with the PR1 loads. The results from JPDF and the NDC clustering analysis are consistent, confirming that CA1 and CA2 are appropriate representation of the data distribution and the two groups present in the data. SPA was lying in between the two groups, where no data exist, i.e., an incorrect representation of both the groups.

Helios again agreed well with one of the two groups on the retreating side. Considering that the SPA showed stall characteristics, an incorrect conclusion would be that Helios failed to capture the stall mechanism. The new clustered results again suggest that there exists a group of cycles (not a subjectively selected individual cycle), matching Helios predictions.

From the validation point of view, several cases of Helios re-

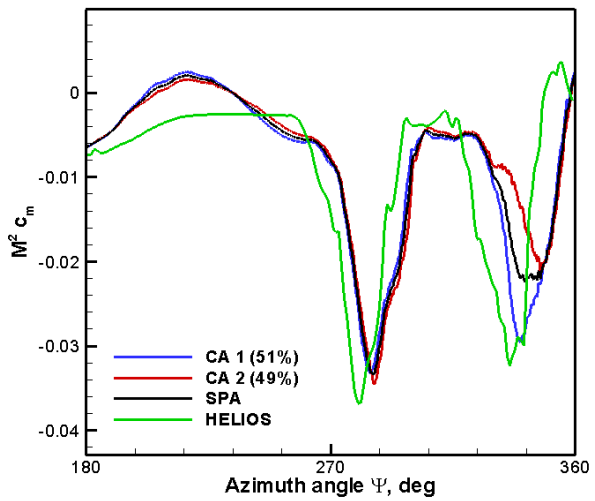

Figure 24. Clustered data at 86.5% radial station for R45P37

sults may have been wrongly judged as over/under predictive of loads, delayed/early stall, or missing wave form (or missing flow phenomena) etc. when compared with the SPA results had it not been for the clustering analysis. Having mentioned that, there are several cases where all the aforementioned issues still exist in terms of predictions that are not shown. The selected Helios cases allowed analyzing the flow field that may have caused clusters in the measured loads. Nevertheless, such improved correlation with one of the two groups (often with the smaller group) allows research to take a different direction. One such example is to identify methods to capture the missing phenomena in Helios that is related to the load characteristics of the large group.

Lastly, results from conducting similar clustering analysis on the torsional moment measured using strain gauges on blade 3 and the correlation with PR3 loads is discussed in the Appendix.

SUMMARY AND CONCLUSIONS

A POD based, data-driven clustering algorithm was applied to the UH-60A wind tunnel data acquired at four high thrust conditions that exhibited higher scatter in general. After validating the clustering algorithm using pushrod load variations caused by known blade-to-blade differences, results were sought for individual pushrod loads, blade surface pressure, sectional loads, and torsional moments. The results confirmed two states, i.e., in and out of stall at constant mean trim conditions. Sectional airloads confirmed that the bimodality in the data is caused by blade sections varying between stalled and unstalled flow conditions. Non-periodic blade-vortex interaction, tunnel variations etc. could have contributed to the observed two states. Nevertheless, cluster-averages with reduced variations compared to the conventional simple phase-average appear to be better representatives of widely varying data. While arguments and analysis to identify the "correct"

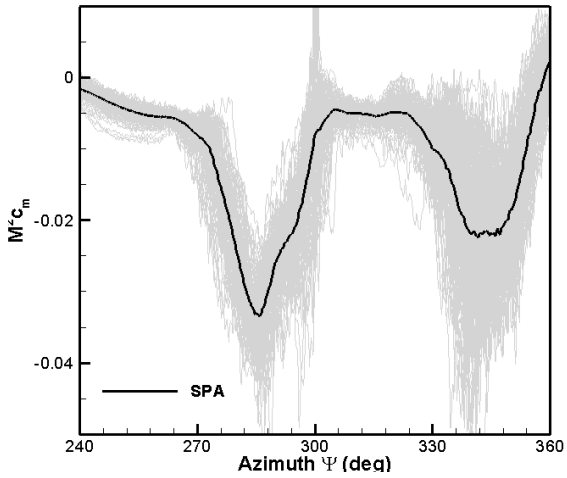

(a) All cycles and SPA

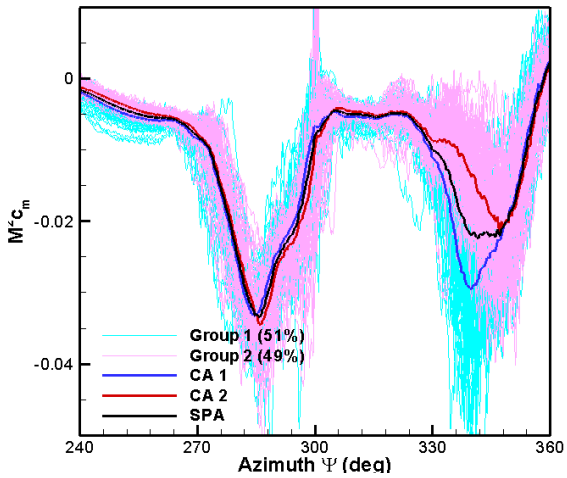

(b) Cluster-averages and SPA

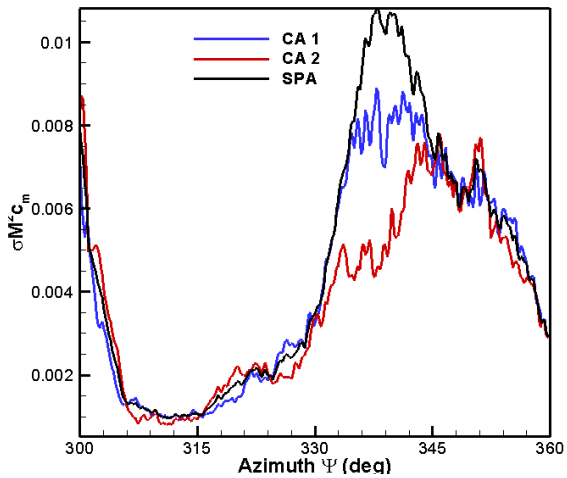

(c) standard deviation

Figure 25. Clustered sectional loads at r/R=0.865 for R45P37

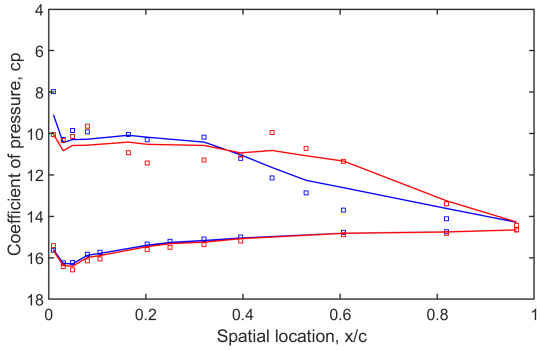

Figure 26. R45P37 - r/R=0.865 cp distribution showing the difference in cluster characteristics.

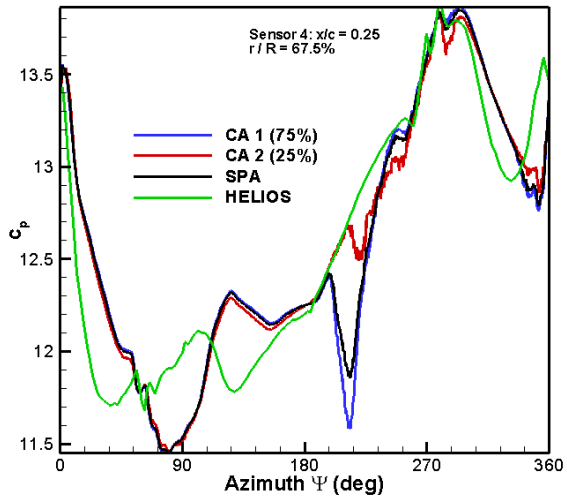

(a) Cp distribution of sensor 4 at 67.5% station

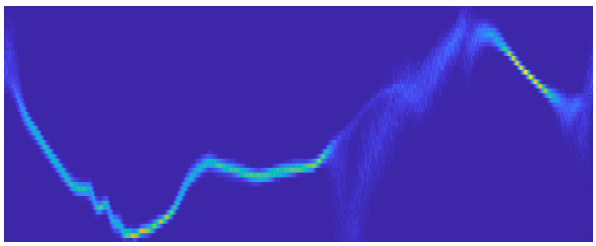

(b) JPDF of cp distribution

Figure 27. Sensor 4 pressure distribution

cluster could be made, recognizing the existence of clusters in the data and using cluster-averages for comparison with analysis is the first step. Comparisons with parametrically varied test data can help determine the validity of the analyses and potentially providing explanations for the predicted accuracies and discrepancies. Helios predictions were first validated using clustered sectional loads. When good correlation was found, simulated flow fields were then used to study the nature of flow experienced by the blade, and hypothesize potential aerodynamic phenomena that may have contributed to the formation of clusters. Following are the specific conclusions derived from the study.

1. Pushrod loads showed the presence of clusters for the higher thrust cases. The average difference in the peak load between the two clusters is about 25%. Compared to the conventional simple phase-average, the peak load for one of the clusters was higher by an average of about 20%. The clusters were unequal in size, and the smaller cluster exhibited more scatter compared to the larger cluster. Nevertheless, separating the data into two groups resulted in a substantial reduction of standard deviation for both the groups compared to the conventional simple phase-average approach that assumes normal distribution in the data set. At the peak load, standard deviation reduced by about 30%. i.e., from 10.5% of the peak load to about 7%. The overall standard deviation at all azimuthal locations reduced by about 8%. A conservative approach to designing pushrod would be to use the cluster-average results that show higher peak load with reduced uncertainty. In the case of validating simulations, cluster-averages, associated variances, and group proportionality are better representatives of measured airload variations than simple phase-average.

2. No clusters were found in the pushrod loads at the lower thrust cases. However, sectional moments still exhibited the presence of clusters. The difference between the unclustered pushrod loads and the clustered sectional moment stem from the asynchronization in the grouped cycles across multiple radial stations. Considering that the sectional loads clusters showed measurable differences, cluster-averages are again better representatives of sectional loads for validating computational simulations appropriately.

3. In the higher thrust cases, remarkable correlation was found between pushrod loads and the surface pressure data that combined all the surface pressure sensors measurements at all radial stations. Such correlation confirm that two different groups indeed exist, and are caused by the local flow conditions (airloads) or the associated aeroelastic response of the blades.

4. Clustering the sectional moments helped to identify the important radial stations that contributed to the clustered pushrod loads. Such stations were identified through the excellent correlation found between the sectional mo-

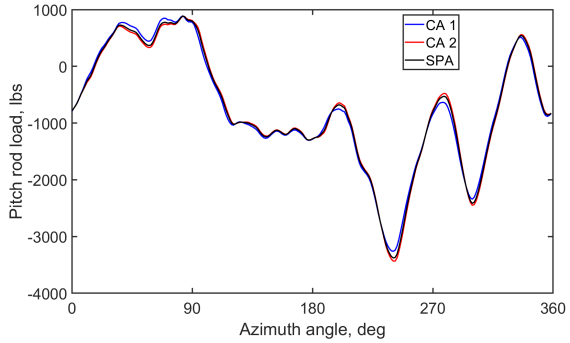

Figure 28. Comparing cluster-averages and phase-average of loads measured using pushrod 3.

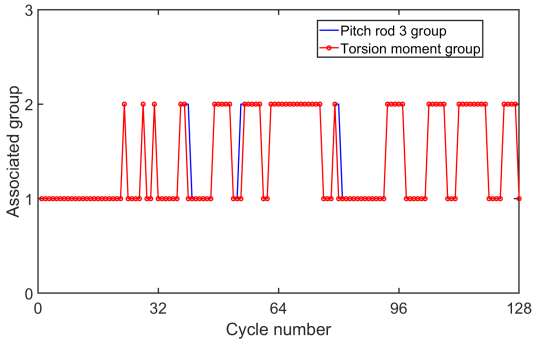

Figure 29. Comparing the clusters found between PR3 and the torsion moment measured using strain gauge data at 40% station

ments and the pushrod loads clusters. In general, clusters causing higher sectional moment are directly related to the higher pushrod load clusters.

5. Chordwise distribution of c_p plotted using clustered data revealed three distinct characteristics of data furcation: (1) presence/absence of stall and separation, (2) chordwise location of separation, and (3) azimuthal location of peak c_m magnitude.

6. Helios predictions showed significantly improved correlation with one of the two groups both at the sectional moment level as well as at the individual surface pressure level. The predictions may have been judged incorrectly as under/over-predicting test results had they been compared to SPA. More importantly, the correlation with one of the clusters enabled studying the flow field corresponding to the cluster. Helios simulations allowed hypothesizing the aperiodicity of trim tab vortices and tip vortices (in terms of strength and spatial location) as one of the aerodynamic phenomena causing clusters in the data.

7. As expected, not all pushrods show identical groups as their flow conditions are different. Pushrod 3 and the torsional moment measured on blade 3 showed excellent correlation in the formation of clusters and the composition of cycles within the clusters.

APPENDIX: TORSIONAL MOMENT CLUSTERS

Similar to PR1, PR3 data alone was analyzed using POD. Figure 28 shows the cluster-averages of the two groups obtained from POD analysis along with the phase-average. While the number of groups is similar to PR1, the number of cycles in each group is different in PR3. The ratio between the two groups is 60% to 40%, compared to nearly 75% to 25% found in PR1. The difference in the peak load between the two groups in PR3 is 285 lbs. The cluster-average 1 peak load was higher than the phase-average peak by about 125 lbs. (or about 4%). Similar to B1, uncertainty in the data can be expected to be lower in the clustered data.

Unlike B1 that also measured surface pressure, B3 measured torsional moments instead. Similar to conducting clustering analysis on the individual radial station surface pressure data (AS1S) on B1, POD results obtained from 40% radial station torsional moment is shown in Fig. 29. Out of 128 cycles, only 5 cycles were different between the two clusters. Again, excellent correlation between two clusters that were obtained from two different measurements measuring two different component of airloads. Comparing blade 1 and blade 3 clusters, the difference in the size of each clusters again highlight the variations between blades.

REFERENCES

1. McCroskey, W. J., "The Phenomenon of Dynamic Stall," NASA TM 81264, March 1981.

2. Carr, L. W., "Progress in the Analysis and Prediction of Dynamic Stall," *Journal of Aircraft*, Vol. 25, (1) , January 1988, pp. 6–17.

3. Le Pape, A., Pailhas, G., David, F., and Deluc, J. M., "Extensive Wind Tunnel Tests Measurements of Dynamic Stall Phenomenon for the OA209 Airfoil Including 3D Effects," Proceedings of the 33rd European Rotorcraft Forum, Kazan, Russia, September 11–13, 2007.

4. Ramasamy, M., Sanayei, A., Wilson, J. S., Martin, P. B., Harms, T., Nikoueen, P., and Naughton, J., "Reducing Uncertainty in Dynamic Stall Measurements Through Data-Driven Clustering of Cycle-To-Cycle Variations," *Journal of the American Helicopter Society*, Vol. 66 (1), January 2021, pp. 1–17. DOI: 10.4050/jahs.66.012003

5. Ramasamy, M., Wilson, J. S., McCroskey, W. J., and Martin, P. B., "Characterizing Cycle-To-Cycle Variations in Dynamic Stall Measurements," *Journal of the American Helicopter Society*, **63**, 022002 (2018), DOI: 4050/JAHS.63.022002.

6. Harms, T., Nikoueeyan, P., and Naughton, J., "Modal Analysis of Cycle-to-Cycle Variations Observed in Dynamic Stall," Proceedings of the 74th Annual Forum and

Technology Display of the American Helicopter Society, Phoenix, AZ, May 14–17, 2018.

7. Lennie, M., Steenbuck, J., Noack, B. R., and Paschereit, C. O., "Cartographing dynamic stall with machine learning," Wind Energy Science Vol. 5 January 2020, pp. 819–830. https://doi.org/10.5194/wes-5-819-2020

8. Piziali, R. A.,"2-D and 3-D Oscillating Wing Aerodynamics For a Range of Angles of Attack Including Stall," NASA TM 4632, USAATCOM TR 940A-011, September 1994.

9. Norman, T. R., Shinoda, P. M., Peterson, R. L., and Datta, A., "Full-Scale Wind Tunnel Test of the UH- 60A Airloads Rotor," American Helicopter Society 67th Annual Forum, Virginia Beach, VA, May 2011.

10. Yamauchi G. K., Wadcock A. J., Johnson W. and Ramasamy M., "Wind Tunnel Measurements of Full-Scale UH-60A Rotor Tip Vortices, American Helicopter Society 68th Annual Forum, AHS Paper 68-2012-000203, Fairfax, VA, 2012.

11. Abrego, A., Meyn, L., Burner, A., Barrows, D., "Final Report on the Full-Scale Blade Displacement Measurements of the UH- 60A Airloads Rotor," AHS Technical Meeting on Aeromechanics Design for Vertical Lift, Holiday Inn at Fisherman's Wharf, San Francisco, CA, January 20-22, 2016

12. Hamade,K., and Kufeld, R., "Modal analysis of UH 60A instrumented rotor blades," NASA TM 4239, November 1990

13. Hartigan, J. A., and Hartigan, P. M., "The Dip Test of Unimodality," *The Annals of Statistics*, Vol. 13, (1), 70-84, March, 1985.

14. Shapiro, S. S., and Wilk, M. B., "An Analysis of Variance Test For Normality," *Biometrika*, Volume 52, (3), 1965, pp 591–611.

15. Sanayei, A., Ramasamy, M., Wilson, J. S., and Martin, P. B., "Development of Modal Analysis Based Clustering Technique Using Pitching Airfoil Measurements," AIAA Paper 2019-1828, Proceedings of AIAA SciTech 2019 Forum, San Diego, CA, January 7–11, 2019.

16. Hamerly, G., and Elkan, C., "Learning the k in k-means," *Advances in Neural Information Processing Systems 16*, MIT Press, NIPS2003-2526, December 2003, pp. 281–288.

17. Ward, J. H., "Hierarchial Grouping To Optimize An Objective Function," *Journal of the American Statistical Association*, Vol. 58, (3), March 1963, pp. 236–244.

18. van der Maaten, L. J. P., and Hinton, G. E., "Visualizing High-Dimensional Data Using t-SNE,". *Journal of Machine Learning Research* Vol. 9, November 2008, pp.2579–2605

19. Johnson, W., "The Effect of Dynamic Stall on the Response and Airloading of Helicopter Rotor Blades," *Journal of American Helicopter Society*, Vol. 14, (2), April 1969, pp. 68–79.

20. Yeo, H., "Investigation of Rotor Airloads and Structural Loads in Maneuvering Flight," Proceedings of the 64th Annual Forum of the American Helicopter Society, Montreal, Canada, April 29-May 1, 2008.

21. Nguyen, K., and Johnson, W., "Evaluation of Dynamic Stall Models with UH-60A Airloads Flight Test Data," Proceedings of the 54th Annual Forum of the American Helicopter Society, Washington, D.C., 20-22 May, 1998.

22. Richez F., Jain R., Smith M., and Grubb A., and Castells C., "Validation and Analysis of Aeroelastic Simulations of the UH-60A Rotor from Pre- to Post-stall Flight Conditions," 76th Annual Forum & Technology Display, Virtual, October 6-8, 2020, Paper Number: 76-2020-0256.

23. Chaderjian, N. M., "Navier-Stokes Simulation of UH-60ARotor/Wake Interaction Using Adaptive Mesh Refinement, Proceedings of the 73rd Annual Forum of the American Helicopter Society, Fort Worth, TX, May 911, 2017

24. Richez, F., "Analysis of Dynamic Stall Mechanisms in He-licopter Rotor Environment," *Journal of the American Helicopter Society*, Vol. 63, (2), 2018, pp. 111.doi: https://doi.org/10.4050/JAHS.63.022006

25. Wissink, A. M., Sitaraman, J., Jayaraman B., Roget, B., Lakshminarayan, V. K., Potsdam M., Jain R., Bauer, A., and Strawn, R., "Recent Advancements in the Helios Rotorcraft Simulation Code," AIAA-2016-0563, AIAA Science and Technology Forum and Exposition (SciTech2016), San Diego, California, January 4-8 2016, https://doi.org/10.2514/6.2016-0563.

26. Nichols, R.H., and Buning, P. G., "OVERFLOW Users Manual, Version 3," April 2020, https://overflow.larc.nasa.gov.

27. Nielsen E. J., Park, M. A., Rumsey, C. L., Thomas, J. L., and Wood, W. A., Biedron, R. T., Carlson, J., Derlaga, J. M., Gnoffo, P. A., Hammond, D. P., Jones, W. T., Kleb B., Lee-Rausch, E. M., "FUN3D Manual: 15," TM 2019-220271, April 2019, https://fun3d.larc.nasa.gov.